Redox Biology 84 (2025) 103649

Contents lists available at ScienceDirect

Redox Biology

journal homepage: www.elsevier.com/locate/redox

PRPS activity tunes redox homeostasis in Myc-driven lymphoma

Austin C. MacMillan [a], Bibek Karki [a], Juechen Yang [b,c], Karmela R. Gertz [a], Samantha Zumwalde [a], Jay G. Patel [a], Maria F. Czyzyk-Krzeska [a,d,e], Jarek Meller [b,c,f], John T. Cunningham [a,*]

[a] *Department of Cancer Biology, University of Cincinnati College of Medicine, Cincinnati, OH, 45267, USA*
[b] *Department of Biostatistics, Health Informatics and Data Sciences, University of Cincinnati College of Medicine, Cincinnati, OH, 45267, USA*
[c] *Division of Biomedical Informatics, Cincinnati Children's Hospital Medical Center, Cincinnati, OH, 45229, USA*
[d] *Veteran Affairs Medical Center, Department of Veterans Affairs, Cincinnati, OH, 45220, USA*
[e] *Department of Pharmacology and System Biology, University of Cincinnati College of Medicine, Cincinnati, OH, 45267, USA*
[f] *Institute of Engineering and Technology, Faculty of Physics, Astronomy and Informatics, Nicolaus Copernicus University, Torun, 87-100, Poland*

ARTICLE INFO

Keywords:
Redox metabolism
Purine metabolism
Pentose phosphate pathway
Mitochondrial respiration
Enzymatic regulation
Oxidative/reductive stress

ABSTRACT

Myc hyperactivation coordinately regulates numerous metabolic processes to drive lymphomagenesis. Here, we elucidate the temporal and functional relationships between the medley of pathways, factors, and mechanisms that cooperate to control redox homeostasis in Myc-overexpressing B cell lymphomas. We find that Myc overexpression rapidly stimulates the oxidative pentose phosphate pathway (oxPPP), nucleotide synthesis, and mitochondrial respiration, which collectively steers cellular equilibrium to a more oxidative state. We identify Myc-dependent hyperactivation of the phosphoribosyl pyrophosphate synthetase (PRPS) enzyme as a primary regulator of redox status in lymphoma cells. Mechanistically, we show that genetic inactivation of the PRPS2 isozyme, but not PRPS1, in Myc-driven lymphoma cells leads to elevated NADPH levels and reductive stress-mediated death. Employing a pharmacological screen, we demonstrate how targeting PRPS1 or PRPS2 elicits opposing sensitivity or resistance, respectively, to chemotherapeutic agents affecting the thioredoxin and glutathione network, thus providing a therapeutic blueprint for treating Myc-driven lymphomas.

1. Introduction

A master transcription factor capable of orchestrating both global and selective transcriptional responses [1–3], the proto-oncogene *c-Myc* rewires metabolic processes en route to oncogenic transformation [4,5]. A well-established hallmark of Myc-dependent metabolic dysregulation is the altered utilization of nutrients such as glucose [6]. Glucose serves as a necessary precursor to fuel Myc-deregulated processes such as nucleotide biosynthesis [7], RNA synthesis [8], protein synthesis [9] and biomass accumulation [10,11]. The global and selective upregulation of these processes is necessary to facilitate the increased anabolic demands of rapidly dividing Myc-overexpressing cells, as increased rates of cell cycle progression and maintenance of cell viability are intimately connected to the Myc-dysregulated metabolic program [12]. While individual Myc-deregulated pathways that contribute biosynthetic precursors, reducing equivalents and bioenergy are separately well-characterized and represent both dependencies and therapeutic vulnerabilities, a comprehensive understanding of their functional coordination in Myc-overexpressing malignancies remains elusive. As a prime example, an oxidative shift has been observed in different types of cancer [13], as bioenergetic processes such as oxidative phosphorylation (OXPHOS) generate products that contribute to oxidative stress [14]. While this oxidative shift is appreciated as a consequence of Myc-driven tumorigenesis that can be leveraged to induce toxic levels of oxidative stress in tumor cells [15–17], the primary mechanisms controlling the temporal and functional coordination between and among Myc-dependent processes that gives rise to altered redox homeostasis are still unclear.

Abbreviations: (oxPPP), oxidative pentose phosphate pathway; (PRPS), phosphoribosyl pyrophosphate synthetase; (OXPHOS), oxidative phosphorylation; (LPS), lipopolysaccharides; (ETC), electron transport chain; (KO), knockout; (WT), wild-type; (OCR), oxygen consumption rate; (ECAR), extracellular acidification rate; (ER), endoplasmic reticulum; (XOR), xanthine oxidoreductase; (ROS), reactive oxygen species; (TRXR), thioredoxin reductase; (GSR), glutathione reductase; (PRPP), phosphoribosyl pyrophosphate; (DTT), dithiothreitol; (NAC), N-acetyl-L-cysteine; (GSH), reduced glutathione; (GSSG), oxidized glutathione.

[*] Corresponding author.

E-mail address: cunnijn@ucmail.uc.edu (J.T. Cunningham).

https://doi.org/10.1016/j.redox.2025.103649
Received 27 March 2025; Accepted 21 April 2025

In this study, we utilize multiple models of Myc-dependent lymphomagenesis to explore the mechanistic underpinnings of Myc-dysregulated redox homeostasis. In Myc-driven B cell lymphomas, overexpression is typically a consequence of a translocation event that repositions the *c-Myc* gene to the immunoglobulin heavy chain enhancer locus of chromosome 14 [18]. We employ the Eμ-Myc mouse model [19] and the P493-6 cell line [20] to model the cellular response to supraphysiological Myc overexpression in B lymphocytes, we use splenic murine (male, 6w) primary B lymphocytes activated with lipopolysaccharides (LPS) as a comparator to induce physiologically relevant enhanced levels of Myc expression, and we utilize the Burkitt's lymphoma-derived CA46 and DG-75 cell lines as models of bona fide Myc-dependent cancer cells. We compile a temporal atlas of the metabolic program under the direct control of oncogenic Myc and identify an early stimulation of oxidative metabolism as the functional consequence of an intricate connection between the mitochondrial electron transport chain (ETC), purine metabolism and the oxidative pentose phosphate pathway (oxPPP). We find that phosphoribosyl pyrophosphate synthetase (PRPS) enzymatic activity functionally links these redox processes, with evolutionarily conserved biochemical differences between the PRPS isoforms governing overall PRPS enzymatic efficiency. We discover that PRPS activity determines PPP flux, serving as an exit valve from the oxPPP and impacting global redox homeostasis in an isoform-specific manner. These metabolic changes are surprisingly uncoupled from Myc-regulated gene expression programs or anabolic processes, and we find that manipulating phosphoribosyl pyrophosphate (PRPP) production via CRISPR/Cas9-based PRPS1 knockout (KO) or PRPS2 KO does not induce sensitivity to inhibitors of nucleotide metabolism. Rather, we demonstrate how inherent differences in PRPS1 and PRPS2 activity can be leveraged to elicit opposing effects on redox homeostasis to selectively target Myc-overexpressing lymphomas with compounds acting on key oxidizing or reducing machineries.

2. Results

2.1. Stimulation of oxidative metabolism is one of the earliest metabolic adaptations to Myc overexpression

We sought to determine the temporal organization of cellular responses (Fig. 1A) to Myc overexpression to better understand how Myc-dysregulated pathways are coordinated to promote global metabolic reprogramming. We first established a catalog of Myc-dysregulated molecular targets and pathways by performing RNA sequencing on murine primary B lymphocytes of the Eμ-Myc mouse model [19], compared to wild-type (WT) mice (Fig. 1B). We next employed the P493-6 human cell line [20] to temporally investigate the relationships between metabolic pathways that were identified as transcriptionally upregulated in the Eμ-Myc mice. We reasoned that a strategy of pairing functional consequences of Myc overexpression with the molecular contributors to the Myc overexpressing cellular phenotype could be used to more accurately define, order and group the key events in the Myc-dependent metabolic program. Consistent with Myc's primary role as a transcription factor and in agreement with other studies [8], one of the earliest events observed was an induction in global transcription within 2 h after Myc induction, evident by increased total RNA content per cell (Supplementary Fig. 1A), levels of nucleotide biosynthetic enzymes and RNA Polymerase I, II and III levels and activation marks (Supplementary Fig. 1B). Interestingly, we identified a stark increase in mitochondrial respiration via oxygen consumption rate (OCR) (Fig. 1C) concurrent with increased nucleotide and RNA synthesis. While the OXPHOS-encoding genes have been identified as downstream targets of Myc in various contexts [21], we observed that many individual components of the nuclear-encoded mitochondrial respiratory complexes maintained consistent levels of expression upon supraphysiological Myc induction (Supplementary Fig. 1C), suggesting that direct regulation of OXPHOS gene expression may not be the primary driver of oxidative metabolism. Additionally, we observed a gradual and sustained increase in both extracellular acidification rate (ECAR) (Fig. 1D) and glucose uptake (Fig. 1E, Supplementary Fig. 1D) over the time course of Myc overexpression which coincided with the Myc-dependent induction of the glycolytic enzymes hexokinase-2 (HK2) and lactate dehydrogenase (LDH) (Fig. 1E). This difference in the regulation of OXPHOS and glycolytic gene behavior is an indication that the Myc-dysregulated program is not an on/off switch, but rather a prioritized temporal activation of distinct interrelated metabolic processes.

4 h after Myc induction, we observed significant increases in cytosolic translation rates (Supplementary Fig. 1E–F) that lagged the induced expression of well-established Myc targets eukaryotic translation initiation factor 4E (eIF4E) and other ribosomal proteins (Supplementary Fig. 1G). Notably, induction of mitochondrial respiration and glycolytic flux preceded the increase in the protein synthesis rate, revealing distinct temporal patterns of Myc-dependent gene expression whereby at least some of the metabolic alterations downstream Myc are controlled by specific gene expression programs rather than being tethered to global increases in anabolism. Coincident with the induction of global translation rates, we observed an expansion of the endoplasmic reticulum (ER) compartment in the absence of an energy stress response (Supplementary Fig. 1H–I), which is consistent with previous findings that suggest a link between increased translation and activation of the unfolded protein response (UPR) in the ER [22]. Notably, murine primary B lymphocytes stimulated with LPS display increased rates of translation at a time point concurrent with that of the P493-6 cells (Supplementary Fig. 1J), but required more time to induce ER expansion and mitochondrial biogenesis (Supplementary Fig. 1K–L). These data establish transcription and stimulation of oxidative metabolism to be the earliest adaptations to Myc-dysregulated metabolism, closely followed by enhanced global translation and organellar biogenesis that occurs after an earlier specific translational response.

2.2. Myc-dependent oxidative metabolism overwhelms the reductive potential of oxPPP-generated NADPH

The early Myc-dependent upregulation of OXPHOS led us to hypothesize that increased respiration may alter intracellular redox homeostasis. To test this, we first performed redox western blotting to assay the oxidative state of xanthine oxidase (XO), a component of the bifunctional xanthine oxidoreductase (XOR) enzyme which oxidizes hypoxanthine during purine catabolism, as well as the mitochondrial-localized thioredoxin 2 (TRX2) and thioredoxin reductase 2 (TRXR2), which utilize the reducing equivalent NADPH to alleviate respiration-linked oxidative stress. We observed a distinct oxidation of reactive cysteines in each these proteins at a time point concurrent with the induction of glucose uptake, though the lack of such shift in cysteine oxidation of the glutathione-dependent glutaredoxin (GLRX) protein hints at selectivity within the Myc-regulated oxidative program (Fig. 1F). We next utilized the AlamarBlue dye as a bio-orthogonal measure of intracellular reductive activity, as the conversion of resazurin to the fluorescent molecule resorufin is primarily reliant upon NAD(P)H-dependent oxidase activity. We did not observe a statistically significant decrease in AlamarBlue fluorescence until 16 h post-Myc induction (Fig. 1G), which was concomitant with an increase in total intracellular and mitochondrial reactive oxygen species (ROS) in both the P493-6 cells (Fig. 1H–I) and LPS-stimulated WT murine primary B lymphocytes (Supplementary Fig. 1M). Despite the pro-apoptotic factor Bim being among the earliest Myc targets to be induced, observable increases in apoptosis via poly[ADP-ribose] polymerase 1 (PARP1) and caspase 3 cleavage are not evident until 12–16 h after supraphysiological Myc overexpression (Supplementary Fig. 1Q), which coincides with the appearance of indicators of oxidative stress and the shift in redox homeostasis. Interestingly, our data illustrates that the Myc-dependent decrease in AlamarBlue reduction is concurrent with the upregulation of kelch-like ECH-associated protein 1 (KEAP1) and

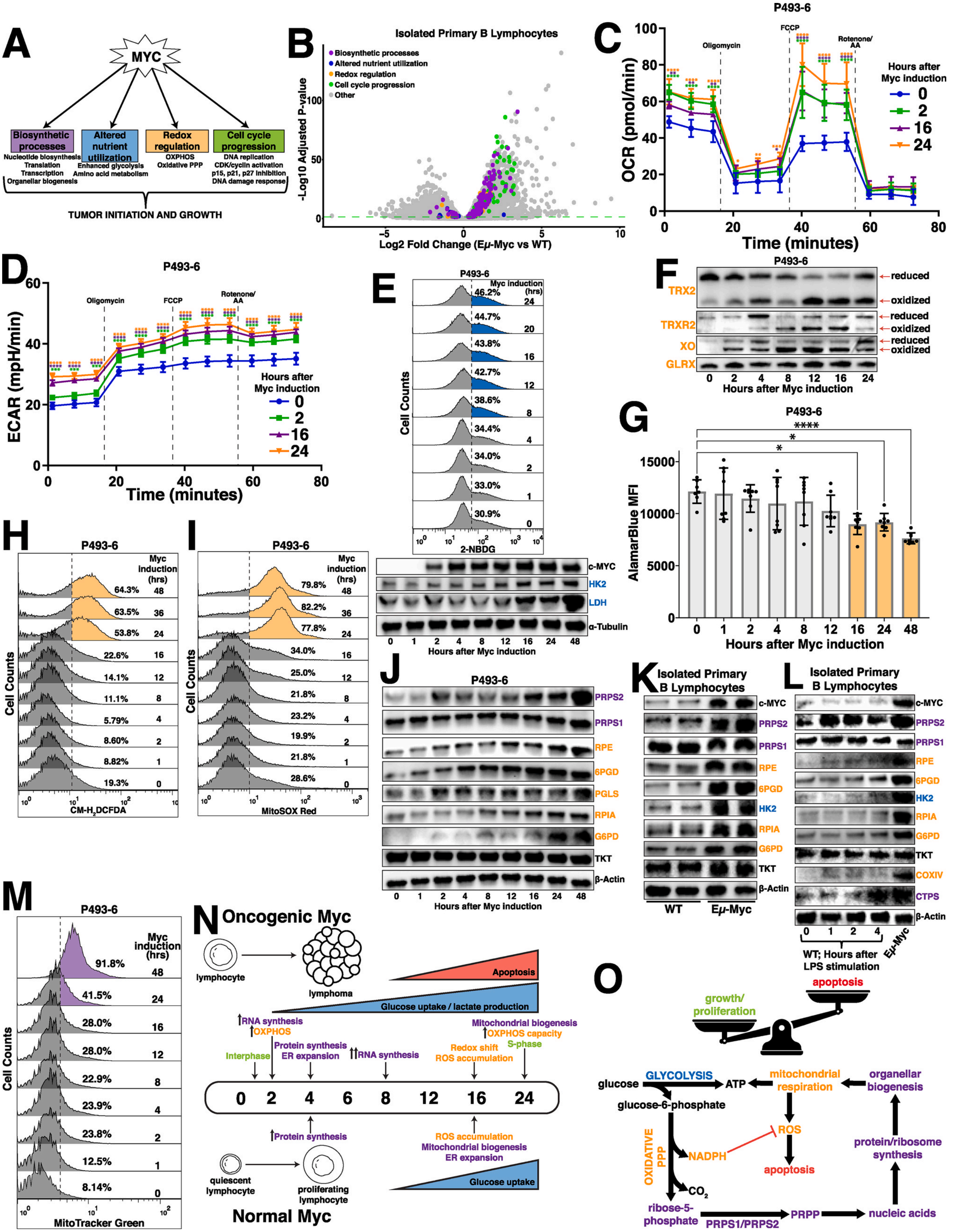

(caption on next page)

Fig. 1. Myc overexpression stimulates oxidative metabolism
(A) Schematic depicting major Myc-dysregulated processes that contribute to tumor initiation and growth.
(B) Volcano plot illustrating differentially expressed genes in Eμ-Myc vs wild-type (WT) murine (male, 6w) primary B lymphocytes (Statistical analysis detailed in Methods; dashed green line demarks significance of $p < 0.05$).
(C) Oxygen consumption rate (OCR) and (D) extracellular acidification rate (ECAR) measured via Seahorse Mito Stress Test in P493-6 cells at times 0hr, 2hr, 16hr and 24hr following tetracycline removal to induce Myc expression. Dashed lines represent the time point at which oligomycin, FCCP and rotenone + antimycin A (AA) were added to the cells.
(E) Glucose uptake in P493-6 cells over a 24hr time course following tetracycline removal to induce Myc expression, measured via 2-NBDG (top). Western blot of glycolytic enzyme expression in P493-6 cells over a 48hr time course following tetracycline removal to induce Myc expression. α-Tubulin used as a loading control (bottom).
(F) Redox western blot illustrating protein oxidation state over a 48hr time course following tetracycline removal to induce Myc expression.
(G) AlamarBlue mean fluorescence intensity (MFI) as a readout of intracellular reduction in P493-6 cells over a 48hr time course following tetracycline removal to induce Myc expression.
(H) Total intracellular reactive oxygen species (ROS) accumulation, measured via CM-H_2DCFDA and (I) mitochondrial ROS accumulation, measured via MitoSOX Red in P493-6 cells over a 48hr time course following tetracycline removal to induce Myc expression.
(J) Western blot of pentose phosphate pathway (PPP) metabolic enzyme expression in P493-6 cells over a 48hr time course following tetracycline removal to induce Myc expression. β-Actin used as a loading control.
(K) Western blot of PPP metabolic enzyme expression in WT and Eμ-Myc murine (male, 6w) primary B lymphocytes. β-Actin used as a loading control.
(L) Western blot of PPP metabolic enzyme expression in WT murine (male, 6w) primary B lymphocytes over a 4hr time course following LPS stimulation. Expression in Eμ-Myc murine (male, 6w) primary B lymphocytes used for comparison. β-Actin used as a loading control.
(M) Mitochondrial mass in P493-6 cells over a 48hr time course following tetracycline removal to induce Myc expression, measured via MitoTracker Green.
(N) Timeline schematizing the temporal activation of metabolic processes following both oncogenic and normal levels of Myc induction.
(O) Schematic depicting routes of glucose utilization to fuel metabolic processes that support lymphoma cell growth and proliferation downstream of oncogenic Myc.
For all panels, statistical analysis performed via one-way ANOVA. Bars represent mean ± s.d.; $^*p < 0.05$, $^{**}p < 0.01$, $^{***}p < 0.001$, $^{****}p < 0.0001$. For all histograms, upregulation quantified as a percentage of the population to the right of the dashed line at each time point.

downregulation of nuclear factor erythroid 2-related factor 2 (NRF2) targets heme oxygenase-1 (HO-1), NAD(P)H:quinone oxidoreductase 1 (NQO1), thioredoxin reductase 1 (TRXR1), TRXR2 and glutathione reductase (GSR) while other established NRF2 targets such as superoxide dismutase 2 (SOD2), thioredoxin 1 (TRX1), catalase, glutamate-cysteine ligase modifier subunit (GCLM) and peroxiredoxin 1 (PRDX1) display no change in expression over the time course of Myc overexpression (Supplementary Fig. 1N), suggesting the NRF2 pathway is not a primary determinant of redox homeostasis under these conditions [23]. Additionally, our data indicates that dehydrogenase-mediated reactions of the tricarboxylic acid (TCA) cycle and folate metabolism are not major contributors to Myc-driven oxidative metabolism, as a majority of the enzymes involved in these pathways display no pattern of upregulation in response to supraphysiological Myc overexpression (Supplementary Fig. 1O).

Because the oxPPP links glucose metabolism and nucleotide biosynthesis while serving as a major source of NADPH production [24] and has been shown to be Myc-regulated in other cancers [5,6], we next sought to assess its potential dysregulation downstream of Myc overexpression. Indeed, we observed an early induction of the PPP enzymes ribulose-5-phosphate-3-epimerase (RPE), 6-phosphogluconate dehydrogenase (6PGD) and 6-phosphogluconolactonase (PGLS) with later induced expression of ribose-5-phosphate isomerase A (RPIA) and glucose-6-phosphate dehydrogenase (G6PD), while the expression of the non-oxPPP enzyme transketolase (TKT) displayed no such upregulation (Fig. 1J). While these findings are consistent in pre-malignant Eμ-Myc murine primary B lymphocytes (Fig. 1K), they are dependent upon supraphysiological levels of Myc expression, as LPS-stimulated WT primary B lymphocytes do not display the same early induction or magnitude of oxPPP gene expression (Fig. 1L). Moreover, the Myc-dependent increase of the NADPH-generating oxPPP enzymes G6PD and 6PGD occurred in the absence of a corresponding increase in transcripts encoding those oxPPP enzymes, implicating transcription-independent roles for Myc during metabolic reprogramming. Importantly, the metabolic effects governing this oxidative shift precede later Myc-dependent changes to mitochondrial biogenesis, as we did not observe a significant accumulation of mitochondrial mass (Fig. 1M) until 24 h after Myc induction, which coincided with an increase in maximum respiratory capacity (Fig. 1C) and S-phase progression (Supplementary Fig. 1P–Q). However, not all organellar biogenesis processes are upregulated downstream of Myc, as there was a slight diminishment of lysosomal content following supraphysiological Myc induction (Supplementary Fig. 1R). Collectively, this analysis establishes a timeline of Myc-dependent metabolic reprogramming (Fig. 1N), where near-immediate activation of the oxPPP directs glucose to nucleotide biosynthesis to facilitate early anabolic processes and provides the reducing equivalent NADPH that can be used to both counteract ROS and augment ETC activity via reactions catalyzed by enzymes such as inosine monophosphate dehydrogenase (IMPDH) and XOR. These results fit a model whereby these metabolic processes sustain lymphoma cell growth and proliferation, which outcompetes the apoptotic phenotype that arises when the reducing capacity generated via oxPPP-mediated NADPH production becomes overwhelmed by the oxidative byproducts of other pathways engaged upon supraphysiological Myc overexpression (Fig. 1O).

2.3. Mitochondrial respiration, purine cycling and oxPPP are intrinsically linked to promote Myc-driven oxidative metabolism

To elucidate which processes are functionally responsible for the increased oxidative metabolism downstream of Myc, we treated P493-6 cells with inhibitors of pathways previously linked to redox homeostasis (Fig. 2A) and conducted a temporal analysis of AlamarBlue reduction. We inhibited OXPHOS in the P493-6 cells by treating with chloramphenicol because the translation of key redox-regulating components of the ETC are mitochondrially-encoded [25,26]; we inhibited oxPPP activity by treating with G6PDi-1 [27] because the oxPPP is a major source of NADPH production and a link has been established between Myc and the oxPPP in some cancers [28]; we inhibited XOR by treating with allopurinol because of its redox bifunctionality as an oxidoreductive enzyme [29] and the studies that have uncovered a connection between purine regulation and mitochondrial metabolism [30,31]; and, we inhibited dihydroorotate dehydrogenase (DHODH) with brequinar because of its function as a mitochondrial membrane-localized oxidoreductive enzyme that transfers electrons to ubiquinol during *de novo* pyrimidine biosynthesis. We observed that treatment with chloramphenicol, G6PDi-1 and allopurinol completely abrogated the Myc-dependent decrease in AlamarBlue fluorescence upon supraphysiological Myc overexpression, whereas treatment with brequinar failed to do so (Fig. 2B). Together, these results pinpoint OXPHOS, purine metabolism and the oxPPP as the major functional determinants of a Myc-driven oxidative program, as inhibiting any of

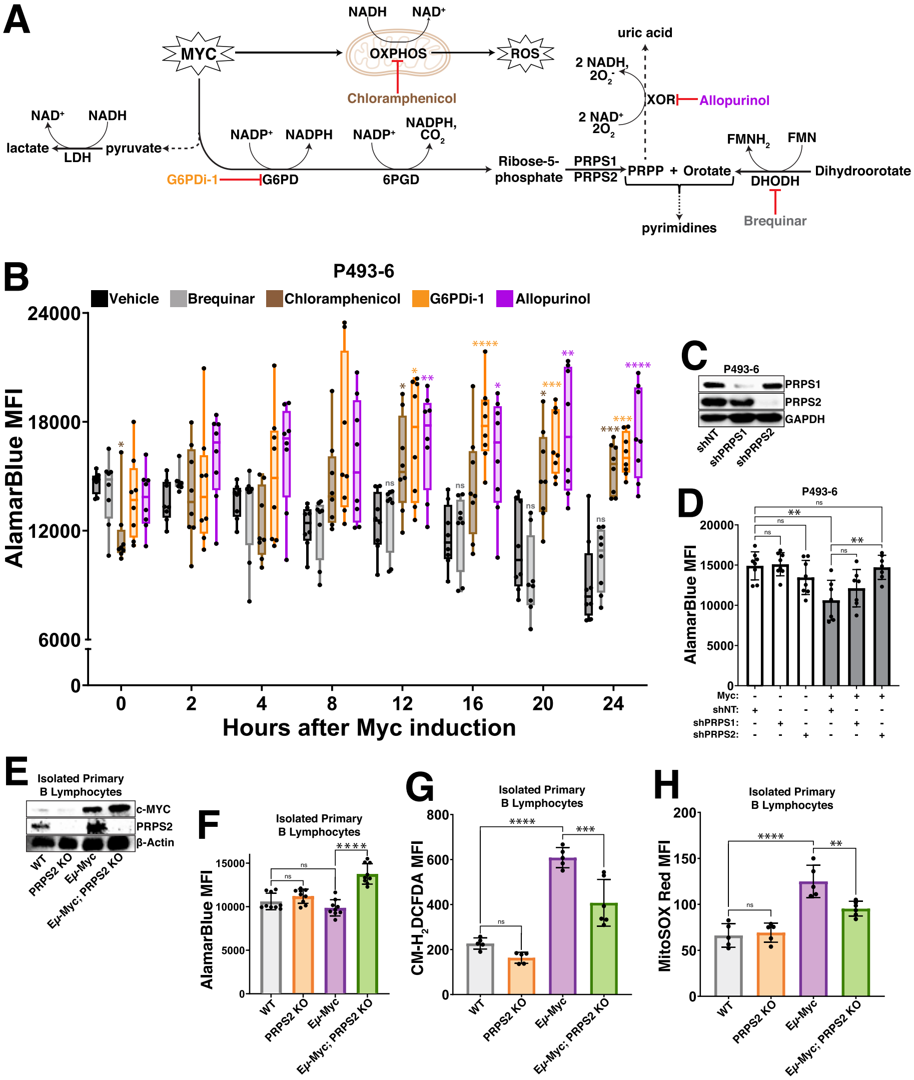

Fig. 2. Myc-dependent coordination of OXPHOS, oxPPP and purine metabolism dictates redox state
(A) Schema for inhibiting major regulators of redox homeostasis downstream of Myc overexpression.
(B) AlamarBlue mean fluorescence intensity (MFI) as a readout of intracellular reduction in P493-6 cells treated with vehicle control (DMSO), brequinar, chloramphenicol, G6PDi-1 or allopurinol over a 24hr time course following tetracycline removal to induce Myc expression.
(C) Western blot validation of shRNA-mediated knockdown of PRPS1 and PRPS2 in P493-6 cells. GAPDH used as a loading control.
(D) AlamarBlue MFI as a readout of intracellular reduction in P493-6 cells under different conditions (Myc OFF, Myc OFF shPRPS1, Myc OFF shPRPS2; Myc ON, Myc ON shPRPS1, Myc ON shPRPS2).
(E) Western blot validation of murine (male, 6w) primary B lymphocyte genotypes. β-Actin used as a loading control.
(F) AlamarBlue MFI as a readout of intracellular reduction in murine (male, 6w) primary B lymphocytes of the indicated genotypes.
(G) Total intracellular ROS accumulation, measured via CM-H_2DCFDA MFI and (H) mitochondrial ROS accumulation, measured via MitoSOX Red MFI in murine (male, 6w) primary B lymphocytes of the indicated genotypes.
For all panels, statistical analysis performed via one-way ANOVA, bars represent mean ± s.d.; *$p < 0.05$, **$p < 0.01$, ***$p < 0.001$, ****$p < 0.0001$, ns: not significant.

these processes abrogates the oxidative shift observed upon Myc induction.

We next sought to determine the metabolic node connecting these redox-regulating processes, where we nominated the PRPS isozymes (PRPS1, PRPS2), which catalyze the conversion of the oxPPP product ribose-5-phosphate (R5P) to the nucleotide biosynthesis pathway intermediate PRPP [32]. We chose these enzymes because of the early induction of PRPS2 expression in response to both supraphysiological and normal levels of Myc overexpression (Fig. 1J–L) and the crucial role of PRPS2 in maintaining lymphoma cell viability [33]. We first confirmed that the PRPS isozymes co-assemble, together with the PRPS associated proteins (PRPSAP1, PRPSAP2), to form a complex [34] in Myc-dependent lymphoma cells (Supplementary Fig. 2A). Interestingly, we observed that the Myc-dependent induction of PRPS2 expression altered PRPS complex configuration, resulting in the downshift of a large molecular weight complex and an enrichment of a smaller molecular weight dimeric configuration between PRPS1 and PRPS2 (Supplementary Fig. 2B). Importantly, this dimeric PRPS configuration suggests a loss of purine-mediated allosteric feedback inhibition, as three subunits of PRPS isozymes are required to create an allosteric binding pocket [35]. To test whether isozyme-dependent remodeling of the PRPS enzyme complex is functionally important for Myc-dependent oxidative metabolism, we performed shRNA-mediated knockdown of PRPS1 and PRPS2 expression in P493-6 cells (Fig. 2C) and compared AlamarBlue reduction ± Myc. We observed no significant change to AlamarBlue conversion upon knockdown of either PRPS isoform in cells

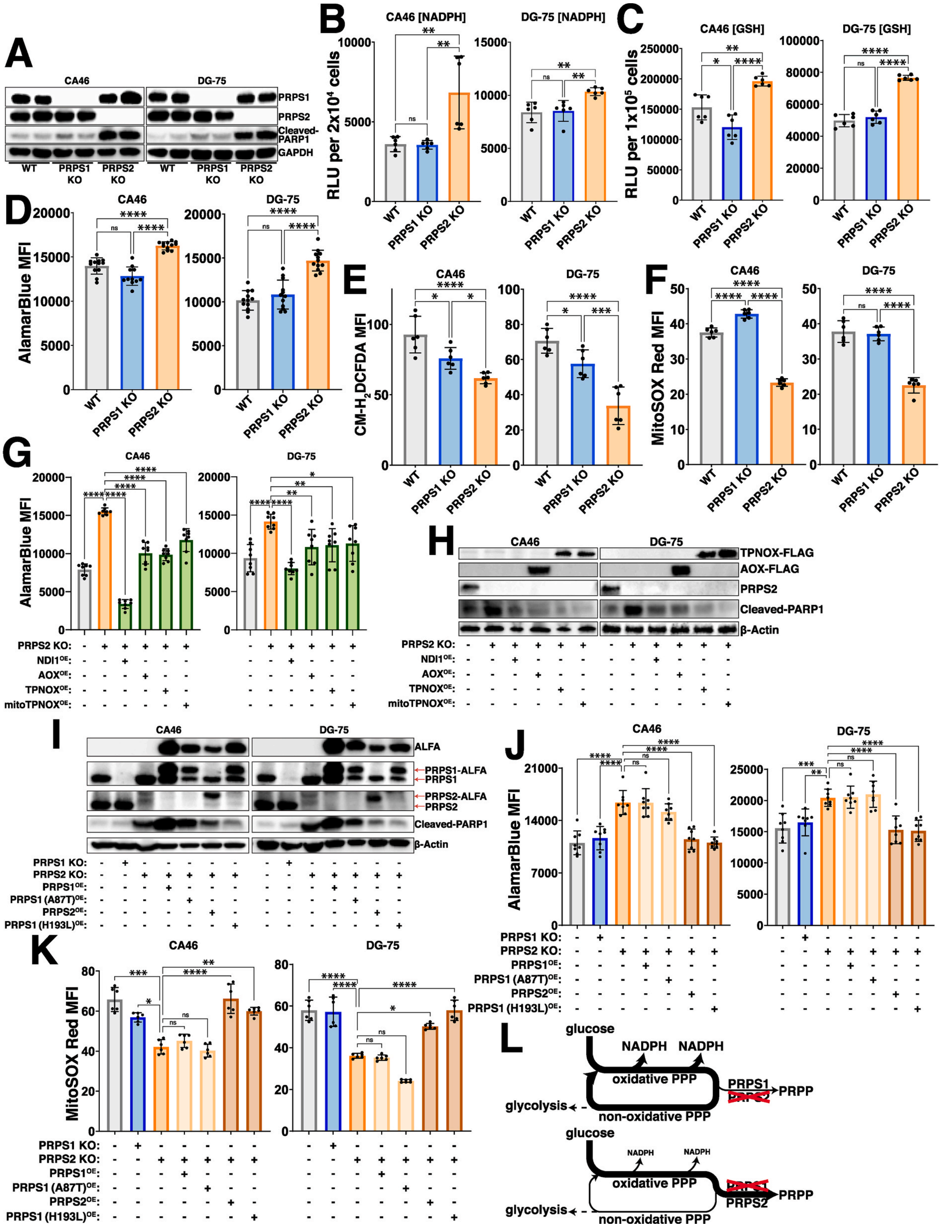

(caption on next page)

Fig. 3. PRPS activity governs redox balance (A) Western blot validating CRISPR/Cas9 mediated knockout of PRPS1 and PRPS2 in two separate human Burkitt's lymphoma-derived cell lines, CA46 (left) and DG-75 (right). 24 kDa PARP1 fragment is used as an apoptotic marker. GAPDH used as a loading control. Levels of (B) NADPH and (C) reduced glutathione (GSH) in WT, PRPS1 KO and PRPS2 KO cells of CA46 (left) and DG-75 (right) cell lines, measured via relative luciferase units (RLU) of luminescent-based GLO-assays. (D) AlamarBlue mean fluorescence intensity (MFI) as a readout of intracellular reduction in WT, PRPS1 KO and PRPS2 KO cells of CA46 (left) and DG-75 (right) cell lines. (E) Total intracellular ROS accumulation, measured via CM-H$_2$DCFDA MFI and (F) mitochondrial ROS accumulation, measured via MitoSOX Red MFI in WT, PRPS1 KO and PRPS2 KO cells of CA46 (left) and DG-75 (right) cell lines. (G) AlamarBlue MFI as a readout of intracellular reduction in WT, PRPS2 KO and PRPS2 KO cells containing exogenously expressed NDI1, AOX, TPNOX or mitoTPNOX of CA46 (left) and DG-75 (right) cell lines. (H) Western blot of PARP1 cleavage as an apoptotic marker in WT, PRPS2 KO and PRPS2 KO cells containing exogenously expressed NDI1, AOX, TPNOX or mitoTPNOX of CA46 (left) and DG-75 (right) cell lines. β-Actin used as a loading control. (I) Western blot validating stable exogenous expression of ALFA-tagged PRPS1, PRPS2 and PRPS1 hypomorphic (A87T) and superactive (H193L) mutant constructs in CA46 (left) and DG-75 (right) PRPS2 KO cell lines. 24 kDa PARP1 fragment is used as an apoptotic marker. β-Actin used as a loading control. (J) AlamarBlue MFI as a readout of intracellular reduction and (K) MitoSOX Red MFI as a readout of mitochondrial ROS accumulation in WT, PRPS1 KO, PRPS2 KO and PRPS2 KO cells containing stably integrated ALFA-tagged PRPS1, PRPS2, PRPS1 hypomorphic (A87T) and superactive (H193L) mutant constructs in CA46 (left) and DG-75 (right) cell lines. (L) Schematic depicting the escape or trapping of glucose-derived carbons in a PPP cycle, governed via PRPS enzymatic efficiency. For all panels, statistical analysis performed via one-way ANOVA, bars represent mean ± s.d.; *$p < 0.05$, **$p < 0.01$, ***$p < 0.001$, ****$p < 0.0001$, ns: not significant.

expressing low levels of Myc, but the decreased levels of AlamarBlue reduction upon supraphysiological Myc overexpression were completely rescued upon knockdown of PRPS2, but not PRPS1 (Fig. 2D). These results were recapitulated in murine primary B lymphocytes (Fig. 2E), where we saw a similar decrease of AlamarBlue reduction (Fig. 2F) paired with significantly elevated levels of both total intracellular (Fig. 2G) and mitochondrial (Fig. 2H) ROS in Eμ-Myc B cells compared to Eμ-Myc; PRPS2 KO B cells. However, no significant change was observed between WT and PRPS2 KO B cells without Myc overexpression. Our previous work found there to be no significant differences between either mitochondrial mass or membrane potential upon PRPS2 KO in either WT or Eμ-Myc B lymphocytes [33], suggesting that the Myc-dependent oxidative program does not require mitochondrial biogenesis but rather activity of the PRPS complex. Together, these data identify OXPHOS, purine metabolism and oxPPP activity as the critical circuitry controlling redox homeostasis in Myc-overexpressing lymphomas and nominate PRPS activity as a central hub coupling these cytosolic and mitochondrial redox processes.

2.4. *PRPS activity couples viability and mitochondrial respiration in Myc-driven lymphoma*

To assess the requirement of Myc-driven, PRPS-dependent redox regulation in the context of fully transformed B cell lymphoma, we generated single-cell selected CRISPR/Cas9 knockouts of both PRPS1 and PRPS2 in CA46 and DG-75 Burkitt's lymphoma-derived cell lines (Fig. 3A). The drastic increase in the cleavage of PARP1 in the PRPS2 KO cells indicates they are significantly more apoptotic, aligning with our previous findings [33]. This phenotype is specific to the Myc-regulated PRPS2 isoform, as knocking out the PRPS1 isoform does not impact viability in these lymphoma cells, suggesting that the Myc-dependent induction of oxidative metabolism may be linked to lymphoma cell viability via PRPS activity. To define the redox alterations upon PRPS2 KO, we measured the levels of key indicators of redox state including NADPH/NADP+ (Supplementary Fig. 2C–D), NADH/NAD+ (Supplementary Fig. 2E–G) and GSH/GSSG (Supplementary Fig. 2H–J). We observed a significant increase in NADPH levels (Fig. 3B), reduced glutathione (GSH) levels (Fig. 3C) and AlamarBlue reduction (Fig. 3D) in the PRPS2 KO cells of both cell lines, while the levels of both total intracellular and mitochondrial ROS were significantly decreased (Fig. 3E–F, Supplementary Fig. 3A–B). We completely restored both the AlamarBlue reduction and viability in the PRPS2 KO cells of each cell line upon exogenous overexpression of NDI1, a single polypeptide encoding the yeast NADH-quinone oxidoreductase enzyme to augment ETC Complex I activity [36], as well as alternative oxidase (AOX), which encodes the terminal oxidase for the ETC in plants [37], indicating a functional coupling between cytosolic and mitochondrial redox networks. We were also able to rescue the NADPH-induced reductive stress of the PRPS2 KO cells with exogenous expression of cytosolic or mitochondrial triphosphopyridine nucleotide oxidase (TPNOX), an engineered *Lactobacillus brevis*-derived oxidase designed to consume intracellular NADPH by catalyzing the reaction $2NADPH + 2H^+ + O_2 \rightarrow 2NADP^+ + 2H_2O$ [38] (Fig. 3G–H). Together, these data confirm an oxidative program in fully transformed Myc-driven lymphoma and suggest that viability and oxidative metabolism are intrinsically linked via PRPS activity.

2.5. *Feedback-refractory biochemical property of PRPS2 promotes the Myc-driven oxidative program*

Though the PRPS isoforms are evolutionarily conserved and exhibit 95 % amino acid sequence identity in humans [34], *in vitro* studies have shown that recombinant PRPS1 isoform is much more sensitive than PRPS2 to inhibition by downstream purine products [32], an allosteric feedback regulatory mechanism found in Class I PRPS enzymes conserved from their bacterial origins [39]. Several disease-causing superactivating mutations in the X-linked *PRPS1* gene that render the PRPS enzyme feedback-refractory to purine-mediated allosteric inhibition have been identified in humans [40]. Of note, the heterozygous H193L mutation was identified in a young female patient, confirming its pathogenicity in the presence of WT PRPS1 and PRPS2 alleles [41]. To test whether differences in allosteric feedback sensitivity to purines account for the phenotypes observed in PRPS2 KO lymphoma cells, we generated ALFA-tagged PRPS1 harboring superactive D52H and H193L mutations to exogenously overexpress in PRPS2 KO cells. To test the alternative hypothesis that PRPS2 upregulation controls enzymatic efficiency of the PRPS complex through structural alterations that are independent of its own enzymatic activity, we engineered a catalytically inactive PRPS2 E39A mutation which renders the enzyme non-functional by abrogating hydrogen bonding between the adenine N6 atom of ATP and the side chain of the evolutionarily conserved glutamic acid at the active site [34]. As an additional negative control, we employed an ALFA-tagged hypomorphic PRPS1 A87T variant which has decreased ATP binding affinity and causes congenital sensorineural hearing loss (DFN2) in humans [42]. Exogenous expression of ALFA-PRPS2 or either of the superactive ALFA-PRPS1 D52H/H193L mutants was sufficient to rescue the viability (Fig. 3I, Supplementary Fig. 3C) and restore the levels of AlamarBlue reduction (Fig. 3J, Supplementary Fig. 3D) and mitochondrial ROS accumulation (Fig. 3K, Supplementary Fig. 3E–F) of PRPS2 KO lymphoma cells, whereas exogenous expression of ALFA-PRPS1, hypomorphic ALFA-PRPS1 A87T or catalytically inactive ALFA-PRPS2 E39A did not. These data support a model by which supraphysiological Myc overexpression selectively upregulates PRPS2, resulting in PRPS2-dependent remodeling of the PRPS complex which feeds oxPPP-derived carbons into purine production and catabolism pathways, to promote OXPHOS and establish and maintain an oxidative metabolic program (Fig. 3L).

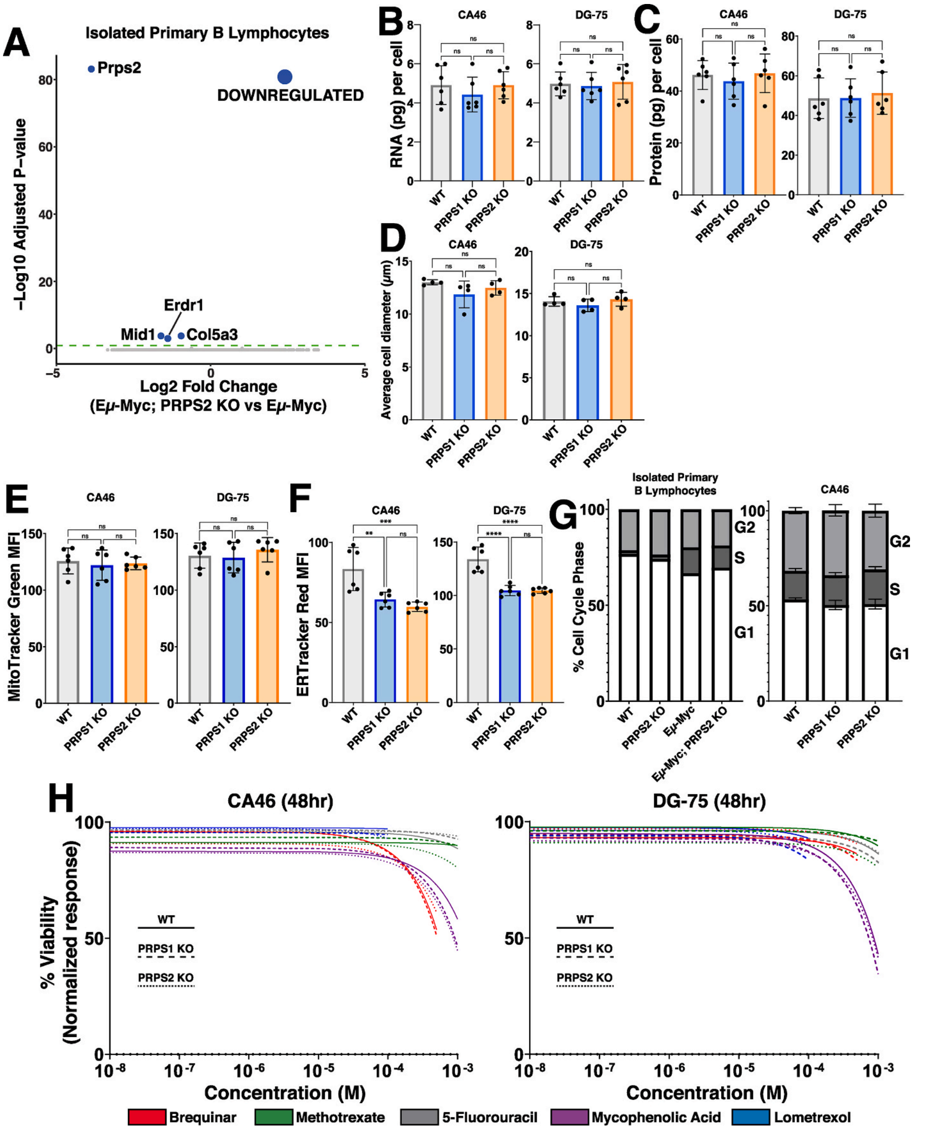

Fig. 4. PRPS activity does not influence anabolic processes or cell cycle

(A) Volcano plot illustrating differentially expressed genes in Eμ-Myc; PRPS2 KO vs Eμ-Myc murine (male, 6w) primary B lymphocyte cells (Statistical analysis detailed in Methods; dashed green line on volcano plot demarks significance of $p < 0.05$).

(B) RNA (pg) content per cell, (C) protein (pg) content per cell and (D) average cell diameter (μm) in WT, PRPS1 KO and PRPS2 KO cells of CA46 (left) and DG-75 (right) cell lines. (E) Mitochondrial mass, measured via MitoTracker Green mean fluorescence intensity (MFI) and (F) ER expansion, measured via ER Tracker Red MFI of WT, PRPS1 KO and PRPS2 KO cells of CA46 (left) and DG-75 (right) cell lines.

(G) Cell cycle analysis profiling the percentage of cells in G1, S, and G2 phases for WT, PRPS2 KO, Eμ-Myc and Eμ-Myc; PRPS2 KO cells of murine (male, 6w) primary B lymphocytes (left) and WT, PRPS1 KO and PRPS2 KO cells of CA46 cells (right).

(H) Dose-response curves illustrating viability response to treatment with 5-fluorouracil, methotrexate, lometrexol, mycophenolic acid and brequinar in WT, PRPS1 KO and PRPS2 KO cells of CA46 (left) and DG-75 (right) cell lines, normalized to vehicle treatment. X-axis represents the logarithmic scale of increasing drug concentration, Y-axis represents the normalized response as a viability percentage. Data was collected 48 h s post-treatment (Data represented as a mean of the normalized viability response of individual replicates at each concentration tested).

For all panels, statistical analysis performed via one-way ANOVA, bars represent mean ± s.d.; $^{**}p < 0.01$, $^{***}p < 0.001$, $^{****}p < 0.0001$, ns: not significant.

2.6. PRPS-dependent control of redox state is uncoupled from Myc-dependent anabolic processes or cell cycle progression

Our temporal analyses indicate that Myc's early gene expression program promotes increased oxPPP flux and PRPP-dependent nucleotide production coincident with an increase in RNA synthesis, so we questioned whether and how PRPS activity is linked to Myc-regulated control of transcription and other anabolic processes. We first performed RNA sequencing in the primary B lymphocytes from pre-malignant Eμ-Myc and Eμ-Myc; PRPS2 KO mice. Of the 4 sufficiently expressed genes found to be differentially regulated ($\log_2$(fold change)≥ 0.95), *Prps2* is the only gene that greatly exceeded the threshold for significance ($p < 0.05$) (Fig. 4A). To test whether PRPS2 KO could counteract Myc's role as global regulator of anabolic metabolism in bona fide models of fully transformed Myc-driven lymphoma, we measured total RNA content per cell (Fig. 4B), protein synthesis rates (Supplementary Fig. 4A), total protein per cell (Fig. 4C), average cell diameter (Fig. 4D) and mitochondrial mass (Fig. 4E), and observed no significant changes upon PRPS1 KO or PRPS2 KO in CA46 and DG-75 cells. ER-tracker staining revealed a decrease in ER content in both PRPS1 KO and PRPS2 KO cells compared to WT, with no significant changes between either KO cell line (Fig. 4F). We assayed the cell cycle

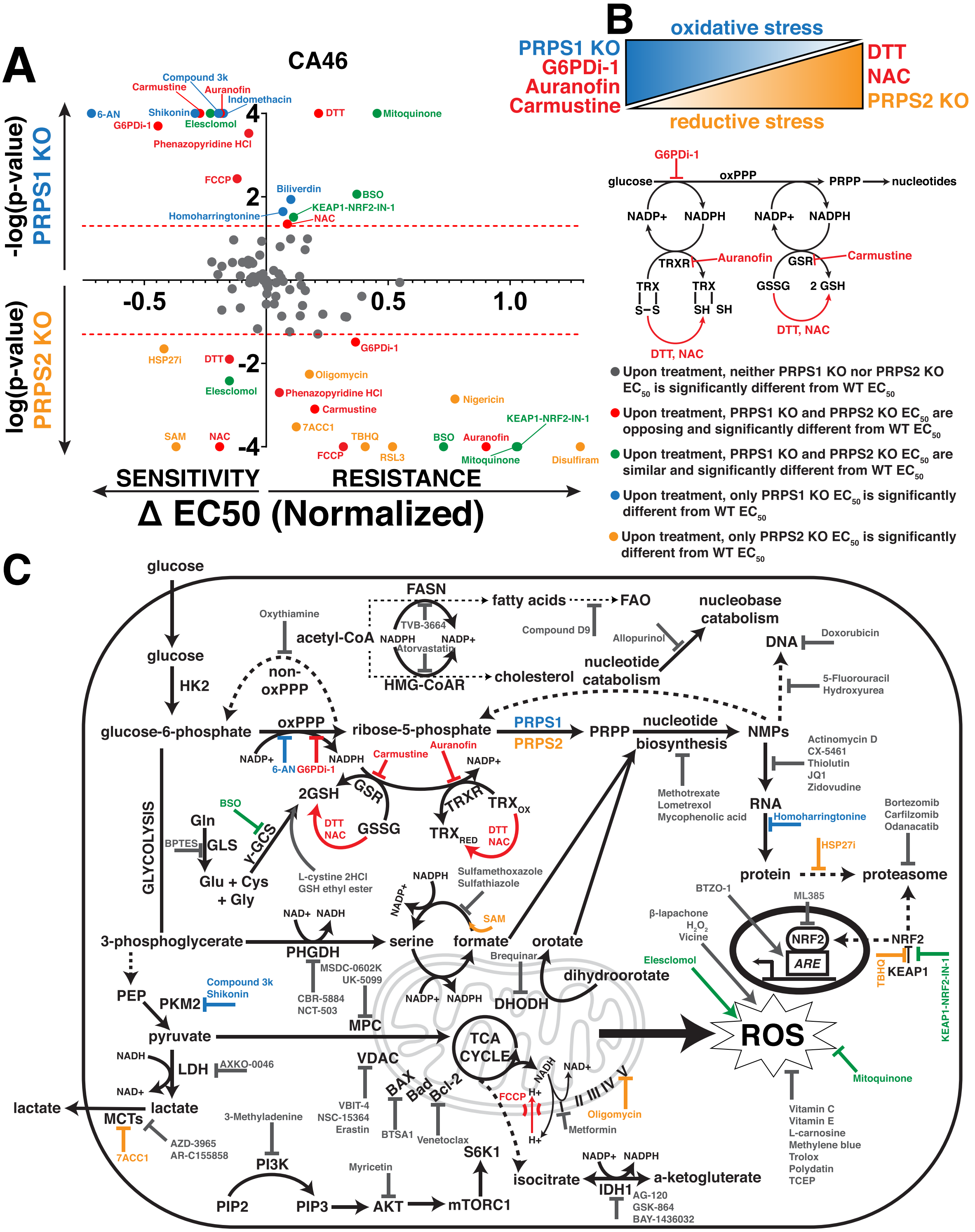

Fig. 5. PRPS-isozyme specific augmentation of redox stress as a therapy

(A) Plot illustrating viability response of PRPS1 KO and PRPS2 KO CA46 cells to treatment with pharmacologic agents, normalized to vehicle treatment. X-axis represents magnitude of EC_{50} change, relative to WT EC_{50}; right side of Y-axis represents resistance to compounds, left side of Y-axis represents sensitivity to compounds. Y-axis represents significance of EC_{50} change plotted as -log(p-value) or log(p-value), compared to WT EC_{50}; PRPS1 KO cells represented above the X-axis, PRPS2 KO cells represented below the X-axis. Significance illustrated by dotted red lines on either side of the X-axis ($p < 0.05$) [EC_{50} and significance determined via nonlinear regression model, fitting a variable slope for (log[x] vs normalized viability response)].

(B) Schema illustrating the combinatorial approach used to generate oxidative stress and reductive stress in CA46 and DG-75 lymphoma cells (top). Schema representing the connection between oxPPP-derived NADPH and the thioredoxin and glutathione antioxidant pathways, with compounds highlighted in red (G6PDi-1, auranofin, carmustine, DTT, NAC) that elicited opposing and significantly differential sensitivities between PRPS1 KO and PRPS2 KO in CA46 and DG-75 lymphoma cell lines.

(C) Schematic representation of functional cooperativity map resulting from pharmacologic screening in CA46 cells.

Color-coded legend provides distinctions for PRPS1 KO or PRPS2 KO EC_{50}, compared to WT EC_{50}.

phase occupancy of both lymphoma cell lines and the murine primary B lymphocytes and observed no consistent changes between cell cycle profiles upon PRPS1 KO or PRPS2 KO (Fig. 4G, Supplementary Fig. 4B), demonstrating that the loss of either PRPS isoform does not interfere with Myc-dependent cell cycle progression. Together, these data demonstrate that despite their essential role in nucleotide production, the cumulative activity of both PRPS enzymes is not required to carry out the global regulation of anabolic processes downstream of Myc hyperactivation. Rather, our data supports a model whereby increased PRPP production downstream of Myc overexpression in PRPS1 KO or PRPS2 KO cells is maintained by adjusting the rate of upstream oxPPP flux, thus explaining the increased concentration of NADPH in PRPS2 KO cells. Our data also indicates that PRPS activity is intrinsically linked to viability and apoptosis despite being uncoupled from Myc-dependent cell cycle progression and growth, suggesting that the perturbations that emerge upon PRPS KO are very specific metabolic effects linked to redox homeostasis.

2.7. Altering PRPP production does not induce sensitivity to inhibitors of nucleotide metabolism

To determine whether altered rates of PRPP production may have a threshold effect to induce sensitivity in Myc-overexpressing lymphomas to inhibitors of downstream PRPP-utilizing pathways, we treated our WT, PRPS1 KO and PRPS2 KO lymphoma cells with the following inhibitors: thymidine nucleotide production (5-fluorouracil; TYMS inhibitor) (Supplementary Fig. 4C), *de novo* pyrimidine biosynthesis (brequinar; DHODH inhibitor) (Supplementary Fig. 4D), *de novo* purine biosynthesis (lometrexol; GART inhibitor) (Supplementary Fig. 4E), folate metabolism (methotrexate; DHFR inhibitor) (Supplementary Fig. 4F), and guanosine nucleotide production (mycophenolic acid; IMPDH inhibitor) (Supplementary Fig. 4G). Not only did these compounds fail to elicit differential responses between WT and PRPS1 KO or PRPS2 KO cells, but they barely impacted viability at the highest concentrations tested. Indeed, only mycophenolic acid treatment achieved a 50 % decrease in viability, which required millimolar concentrations of the drug (Fig. 4H). These findings that altering PRPP production via PRPS1 KO or PRPS2 KO does not induce sensitivity to inhibitors of nucleotide metabolism could perhaps be explained by a combination of decreased nucleotide catabolism and increased nucleotide salvage. These data demonstrate that targeting a single pathway of PRPP utilization is therapeutically insufficient, even in the context of PRPS1 KO or PRPS2 KO, reinforcing the concept that Myc-overexpressing cell viability is linked to redox homeostasis. These results also emphasize the importance of sustaining PRPP production, and demonstrate how Myc-overexpressing lymphomas adjust flux to accommodate more or less efficient PRPS complex configurations. Together, these findings underscore the difficulty in targeting the more aggressive, therapy-refractory tumors characterized by Myc hyperactivation, which exhibit tremendous metabolic flexibility by virtue of the myriad deregulated pathways that provide redundancy and resiliency [43].

2.8. PRPS-isozyme specific regulation reveals vulnerabilities in thioredoxin, glutathione redox pathways

To identify metabolic pathways and targets that elicit significant and differential responses between WT and PRPS KO lymphoma cells, we curated a library of over 100 different compounds with mechanisms of action involving metabolic processes (antioxidant properties, protein homeostasis, transcription, heme metabolism, lipid metabolism, glucose metabolism and apoptosis) and specific classes of enzymes (dehydrogenases, kinases and transporters) to pinpoint which Myc-dysregulated metabolic pathways could be leveraged as a combinatorial therapeutic approach (Supplementary Table 1). Each compound was tested at increasing concentrations in WT, PRPS1 KO and PRPS2 KO CA46 lymphoma cells such that normalized viability responses could be reported as an EC_{50} value. The results of this screening are displayed in Fig. 5A, with the response to treatment of each compound represented as ΔEC_{50} magnitude vs ΔEC_{50} significance in PRPS1 KO and PRPS2 KO cells. Of all the compounds tested in the CA46 lymphoma cell line, we found 7 that yielded both statistically significant and opposing sensitivities between PRPS1 KO and PRPS2 KO cells compared to WT cells, 5 of which recapitulated their behavior in DG-75 cells: dithiothreitol (DTT), N-acetyl-L-cysteine (NAC), G6PDi-1, carmustine and auranofin. Of these 5 compounds, DTT and NAC both function as reducing agents [44,45] and both sensitized PRPS2 KO cell viability compared to WT controls, while PRPS1 KO cells were more protected against cell death upon their treatment. This data suggests that DTT and NAC are more effective against Myc-overexpressing PRPS2 KO lymphoma cells because they exacerbate reductive stress [46]. Conversely, we found G6PDi-1, carmustine and auranofin all to be more toxic to PRPS1 KO cells compared to WT controls, whereas PRPS2 KO cells were more protected against cell death upon treatment. These compounds all create a more oxidative intracellular environment; G6PDi-1 suppresses NADPH production via blocking the first step in the oxPPP [27], carmustine prevents the conversion of GSSG to GSH via carbamoylation of GSR [47], and auranofin works in a similar fashion by preventing the reduction of thioredoxin disulfide bonds via inhibition of TRXR [48]. Importantly, the NADPH produced via G6PD is the reducing equivalent required to drive the reactions catalyzed by both GSR and TRXR, indicating that these pathways are intertwined to suppress oxidative stress (Fig. 5B).

The results from the screening are schematized in a functional cooperativity map (Fig. 5C), which represents a majority of the compounds tested and pathways affected based on the response or lack thereof in PRPS1 KO or PRPS2 KO CA46 cells compared to WT CA46 cells to establish key takeaways. Inhibiting NAD+/NADH-dependent dehydrogenase activity of enzymes such as IMPDH, LDH, phosphoglycerate dehydrogenase (PHGDH) and isocitrate dehydrogenase (IDH) resulted in no significant ΔEC_{50} between PRPS1 KO, PRPS2 KO or WT cells. The significant and differential responses upon inhibition of G6PD, GSR and TRXR seem to be restricted to the glutathione and thioredoxin antioxidant systems, as inhibiting other NADP+/NADPH-dependent processes such as fatty acid synthase (FASN) and hydroxymethylglutaryl-coenzyme A reductase (HMG-CoAR) did not elicit differential responses upon treatment. These results are also specific to the NADPH-dependent reductive activity of the enzymes and not the presence of the antioxidant molecule GSH, as evidenced by a lack of differential response upon treatment with BSO, GSH ethyl ester or L-cystine 2HCl. Though many ROS-modulating compounds were tested, only NAC and DTT were found to generate significant differential sensitivities upon treatment in both cell lines. NRF2 activation or inhibition both failed to create differential sensitivities between KO cells, which aligns with our data suggesting that the KEAP1-NRF2 axis is not the primary effector for Myc-driven oxidative metabolism (Supplementary Fig. 1N). These data suggest that the effects revealed upon treatment with redox-modifying compounds are not a general phenomenon, but rather a very selective response. Also in line with our data (Fig. 4H), we observed that compounds interfering with different nodes of anabolic metabolism such as nucleotide metabolism, RNA synthesis and protein homeostasis did not reveal any significant and differential sensitivities between PRPS1 KO and PRPS2 KO cells, compared to WT cells. Additionally, no significant differential sensitivities were discovered when treating with inhibitors of pro- or anti-apoptotic proteins, mitochondrial membrane-bound transporters or mammalian target of rapamycin complex 1 (mTORC1) signaling. These data nominate the PRPS1 isozyme as a completely new potential therapeutic target in Myc-overexpressing lymphomas, as PRPS1 KO cells are sensitive to oxidative stressors that specifically interfere with the NADPH-dependent reductive activity of the thioredoxin and glutathione pathways. They also nominate PRPS2 ablation as a genetic tool to leverage alone or in combination with other reducing agents to generate toxic levels of reductive stress.

2.9. Tuning PRPS activity as a therapeutic approach in Myc-overexpressing lymphoma

To test our model that PRPS1-dependent feedback sensing is a throttle on PRPS activity, thereby stifling oxPPP flux in lymphocytes, we assessed the ability of PRPS1 hypomorphic (A87T), superactive (D52H, H193L) and PRPS2 catalytically inactive (E39A) variants to rescue the differential sensitivities upon treatment with the 5 compounds that emerged from our screening. We observed that exogenous overexpression of PRPS2 and the superactive PRPS1 D52H and H193L mutants largely, if not completely, re-sensitized PRPS2 KO lymphoma cells to treatment with auranofin (Supplementary Fig. 5A), carmustine (Supplementary Fig. 5B) and G6PDi-1 (Supplementary Fig. 5C), while exogenous overexpression of PRPS1, hypomorphic PRPS1 A87T and catalytically inactive PRPS2 E39A failed to do so. In contrast, exogenous PRPS2 overexpression and superactive PRPS1 D52H and H193L mutants largely, if not completely, rescued the induced sensitivity of PRPS2 KO to treatment with DTT (Supplementary Fig. 5D) and NAC (Supplementary Fig. 5E), while exogenous overexpression of PRPS1, hypomorphic PRPS1 A87T and catalytically inactive PRPS2 E39A failed to do so. To rule out alternative mechanisms of toxicity linked to changes in redox, we assayed our cell lines for lipid peroxidation (Supplementary Fig. 5F), labile iron accumulation (Supplementary Fig. 5G) and global protein oxidation (Supplementary Fig. 5H), which failed to demonstrate a consistent and significant response between WT and PRPS KO lymphoma cells. Taken together, these data imply an exquisite specificity to the thioredoxin and glutathione networks within the Myc-regulated redox program comprised of the oxPPP-purine metabolism-OXPHOS circuit.

3. Discussion

It's been known for decades that Myc stimulates mitochondrial respiration and oxidative metabolism, with recent studies leveraging this knowledge to demonstrate the therapeutic benefit of attacking this core feature of Myc's metabolic program [15–17]. Here, we unravel the mechanistic circuitry underlying the altered oxidative homeostasis, and in the process identify an important connection between cytosolic and mitochondrial redox metabolism. As lymphocytes are among the most rapidly proliferating cells in the body, replicating as quickly as 9 h after the initial cell division [49], *c-Myc* has also been shown to play an indispensable role in normal B cell activation and proliferation as a transcriptional amplifier with a core function in regulating the rate of nucleotide production [50]. Recent studies have also implicated oxidative metabolism as an essential component of B cell development by promoting selection, maturation and class-switch recombination of B cells [51,52]. Our data lends mechanistic support to these studies, suggesting that Myc engages OXPHOS machinery as one of the earliest metabolic alterations to exacerbate oxidative metabolism in lymphoma cells, simultaneous with that of nucleotide biosynthesis and transcription. Our work may also help explain observations regarding genetic disorders of the immune compartment such as severe combined immunodeficiency (SCID) [53], Arts syndrome [54], Charcot-Marie-Tooth disease-5 (CMTX5) [55], DFN2 [42] and lupus erythematosus [56] some of which are X-linked disorders arising from mutations in PRPS1 or PRPS2. Additionally, we provide mechanistic insight to help explain the immunosuppressive effects of pharmacological agents that target lymphocytes such as mycophenolic acid [57] and mizoribine [58] (IMPDH), allopurinol (XOR) [59] and auranofin (TRXR) [60]. Our work functionally connects primary redox circuitries and helps explain these genetic and pharmacological observations, magnifying the critical balance of purine production and catabolism to maintain oxidative metabolism and overall immune competency of lymphocytes.

Our data demonstrates that supraphysiological levels of Myc activation generates oxidative stress, which has been shown to promote pro-tumorigenic processes such as proliferation, migration, angiogenesis, drug resistance and genomic instability in different cancers [13]. We show that induction of the oxPPP is concomitant with that of OXPHOS and serves a dual role in producing nucleotides and combatting ROS to sustain TRX and GSH. Our data is consistent with a model whereby the PPP functions as a cycle, its flux principally governed by the PRPS enzymes which serve as exit valves. Importantly, the PRPS enzymes and regulatory PRPSAPs exist in a dynamic megadalton multimeric assembly in lymphocytes that catalyzes the conversion of R5P to PRPP. Our group has established an evolutionary timeline for the origin of PRPS complex members and derived a model of PRPS complex assembly, where we discovered that the PRPS2 isoform arose from a gene duplication event where it diverged from and lost some of the allosteric feedback sensitivity of the ancestral PRPS1 isoform [34]. Here, we establish PRPS1 KO cells have lost the evolutionarily conserved allosteric brakes from the PRPS complex, permitting enhanced flux through the oxPPP to foster PRPS2-dependent nucleotide production. In PRPS2 KO cells however, these allosteric brakes are preserved, forcing enhanced cycling through the oxPPP which increases NADPH production as a byproduct of sustaining sufficient levels of PRPP and downstream nucleotides. Furthermore, we show that Myc-dependent upregulation of PRPS2 alters overall PRPS complex configuration, favoring a smaller dimeric assembly between PRPS1 and PRPS2 as opposed to the larger molecular weight complex that has been identified in Myc-low cells. These findings combine to suggest that the PRPS1:PRPS2 ratio is tunable to regulate overall PRPS activity based on the cell's metabolic needs, with our data demonstrating that Myc overexpression favors an increase in PRPS2: PRPS1 to increase PRPS activity via the purine feedback insensitive PRPS2 isoform to enhance purine cycling and mitochondrial respiration.

4. Conclusions

The results of these findings nominate the PRPS isozymes as critical regulators of redox homeostasis in Myc-overexpressing lymphomas, which is uncoupled from Myc-dependent regulation of transcription, cell cycle control or other anabolic processes. We nominate a unique combinatorial therapeutic approach to take advantage of the Myc-dependent oxidative metabolism required for proliferating B cells, leveraging PRPS isoform-specific alterations in redox homeostasis to exacerbate vulnerabilities. Specifically, we discover that oxPPP-derived NADPH is necessary to drive the reactions catalyzed by TRXR and GSR, identifying inhibition of the PRPS1 isoform as a new potential therapeutic angle to sensitize cells to toxic levels of oxidative stress in these lymphomas. Conversely, while triggers of reductive stress-mediated cell death remain elusive due to a lack of appropriate markers and readouts [46], we uncovered one of the few known loss-of-function genetic approaches to induce reductive stress (PRPS2 KO) and outlined a therapeutic approach combining reducing agents with PRPS2 KO to create toxic levels of reductive stress. Overall, this study highlights PRPS activity as the molecular rheostat dictating the redox state in Myc-driven lymphomas and provides a proof-of-concept in how the tunability of a metabolic enzyme may be exploited for therapeutic benefit in Myc-driven lymphoma.

Quantification and statistical analysis

Countess II FL was used in conjunction with Trypan blue for all cell counting and analysis of cell size. MARS Data Analysis Software was used for the collection of all data obtained via the BMG Labtech CLARIOStar microplate reader. FlowJo was used for the analysis of all (.fcs) files obtained via flow cytometry. GraphPad Prism was used for the normalization, statistical analysis, and plotting of all data sets. Agilent XFe96 Seahorse Analyzer was used in conjunction with Agilent WAVE software to conduct and collect data from Seahorse experiments. Bio-Rad ChemiDoc Touch Imaging System and Bio-Rad ImageLab were used for the acquisition and representation of all chemiluminescent Western Blot images. Adobe Illustrator was used to compile and generate all figures in their final form. Unless otherwise specified, $n \geq 3$

replicates were used per experiment, with one-way ANOVA statistical test used to determine significance for all quantitative data except for dose-response curves, where a nonlinear regression model fitting a variable slope for (log[x] vs normalized viability response) was used to determine EC_{50} and significance. For all statistical analyses, asterisks representing p values are indicated in each figure legend, with ns indicating "not significant" ($p > 0.05$).

Lead contact

Further information and requests for reagents should be directed to, and will be fulfilled by, the lead contact, John T. Cunningham (cunnijn@ucmail.uc.edu).

Materials availability

All unique reagents generated in this study will be made available by the lead contact upon request with a completed Materials Transfer Agreement.

Data availability

- All data supporting the findings of this study are available within the Article and its Supplementary Information. Raw and processed RNA sequencing data may be obtained via accession no. GSE282435 at https://www.ncbi.nlm.nih.gov/geo/query/acc.cgi?acc=GSE282435.
- This paper does not report original code.

Funding

This work was supported by the National Institutes of Health [R01CA230904 (JTC); R35GM133561 (JTC); 5T32ES007250-34 (KRG); R01CA287260 (MCK)]; the U.S. Department of Veterans Affairs [2I01BX001110 BLR&D VA Merit Award (MCK)]; and the National Cancer Institute [R25CA261610 (JGP)].

CRediT authorship contribution statement

Austin C. MacMillan: Conceptualization, Data curation, Formal analysis, Investigation, Methodology, Validation, Visualization, Writing – original draft, Writing – review & editing. **Bibek Karki:** Data curation, Formal analysis, Investigation, Methodology, Validation, Visualization, Writing – review & editing. **Juechen Yang:** Data curation, Formal analysis, Software, Visualization. **Karmela R. Gertz:** Funding acquisition, Investigation, Writing – review & editing. **Samantha Zumwalde:** Investigation. **Jay G. Patel:** Funding acquisition, Investigation. **Maria F. Czyzyk-Krzeska:** Funding acquisition, Resources, Supervision. **Jarek Meller:** Resources, Software, Supervision. **John T. Cunningham:** Conceptualization, Funding acquisition, Investigation, Methodology, Project administration, Resources, Software, Supervision, Validation, Visualization, Writing – original draft, Writing – review & editing.

Declaration of competing interest

The authors declare the following financial interests/personal relationships which may be considered as potential competing interests: ACM and JTC have filed a patent application on this work. All other authors declare no competing interests.

Acknowledgements

We thank the Transgenic Animal and Genome Editing (TAGE) core at the Cincinnati Children's Hospital Medical Center (CCHMC) for the generation of the PRPS2 KO mouse strain used for this research project, which was created from ES cell clone $PRPS2^{tm1a(KOMP)Wtsi}$ (EPD0110_2_A05) obtained from KOMP Repository (www.komp.org) and generated by the Wellcome Trust Sanger Institute. We thank the Genomics, Epigenetics and Sequencing (GES) core at the University of Cincinnati for conducting RNA sequencing. We thank B. Ehmer for assistance with the training, maintenance and oversight of flow cytometry equipment in the Advanced Cell Analysis Service Center (ACASC) at the University of Cincinnati, College of Medicine. We thank K. Patra, C. Andreani and C. Bartolacci for their insights during the manuscript review process.

Appendix A. Supplementary data

Supplementary data to this article can be found online at https://doi.org/10.1016/j.redox.2025.103649.

Materials & Methods

Key Resource Table

	SOURCE	IDENTIFIER
Antibodies		
Rabbit polyclonal anti-c-Myc	Cell Signaling Technology	Cat #9402; RRID:AB_2151827
Rabbit monoclonal anti-ACLY	Cell Signaling Technology	Cat #13390; RRID:AB_2798203
Mouse monoclonal anti-ATIC	Abcam	Cat #ab33520; RRID:AB_725572
Rabbit polyclonal anti-RRM2	Novus Biologicals	Cat #NBP1-31661; RRID:AB_2180393
Rabbit monoclonal anti-eIF4E	Cell Signaling Technology	Cat #2067; RRID:AB_2097675
Rabbit polyclonal anti-NPM	Cell Signaling Technology	Cat #3542; RRID:AB_2155178
Mouse monoclonal anti-NDUFA9	Abcam	Cat #ab14713; RRID:AB_301431
Rabbit monoclonal anti-SDHA	Cell Signaling Technology	Cat #11998; RRID:AB_2750900

(*continued on next page*)

(*continued*)

	SOURCE	IDENTIFIER
Mouse monoclonal anti-UQCRC1	Thermo Fisher Scientific	Cat #459140; RRID:AB_10375175
Rabbit recombinant anti-COX IV	Abcam	Cat #ab202554; RRID:AB_2861351
Mouse monoclonal anti-ATP5A	Abcam	Cat #ab14748; RRID:AB_301447
Rabbit monoclonal anti-BiP	Cell Signaling Technology	Cat #3177; RRID:AB_2119845
Rabbit monoclonal anti-Cleaved PARP-1	Abcam	Cat #ab32064; RRID:AB_777102
Rabbit recombinant monoclonal anti-β-Actin	Cell Signaling Technology	Cat #4970; RRID:AB_2223172
Mouse monoclonal anti-β-Actin	Cell Signaling Technology	Cat #3700; RRID:AB_2242334
Rabbit monoclonal anti-Rpb1 CTD (phospho-Ser2)	Cell Signaling Technology	Cat #13499; RRID:AB_2798238
Rabbit monoclonal anti-Rpb1 CTD (phospho-Ser5)	Cell Signaling Technology	Cat #13523; RRID:AB_2798246
Rabbit monoclonal anti-Rpb1 CTD (phospho-Thr4)	Cell Signaling Technology	Cat #26319; RRID:AB_2798921
Mouse monoclonal anti-Rpb1 CTD	Cell Signaling Technology	Cat #2629; RRID:AB_2167468
Rabbit monoclonal anti-POLR1A	Cell Signaling Technology	Cat #24799; RRID:AB_2798884
Rabbit monoclonal anti-POLR3A	Cell Signaling Technology	Cat #12825; RRID:AB_2798036
Rabbit polyclonal anti-Histone H3 (acetyl-Lys27)	Cell Signaling Technology	Cat #4353; RRID:AB_10545273
Rabbit monoclonal anti-RPE	Abcam	Cat #ab128891; RRID:AB_11140856
Rabbit monoclonal anti-PGD	Abcam	Cat #ab129199; RRID:AB_11144133
Rabbit polyclonal anti-PGLS	Abcam	Cat #ab135771
Rabbit monoclonal anti-HK2	Cell Signaling Technology	Cat #2867; RRID:AB_2232946
Mouse monoclonal anti-RPIA	Santa Cruz Biotechnology	Cat #sc-515328
Mouse monoclonal anti-PRPS1/2/3	Santa Cruz Biotechnology	Cat #sc-376440; RRID:AB_11151043
Mouse monoclonal anti-G6PD	Santa Cruz Biotechnology	Cat #sc-373886; RRID:AB_10918100
Rabbit monoclonal anti-KEAP1	Cell Signaling Technology	Cat #8047; RRID:AB_10860776
Rabbit monoclonal anti-HO-1	Cell Signaling Technology	Cat #43966; RRID:AB_2799254
Mouse monoclonal anti-NQO1	Santa Cruz Biotechnology	Cat #sc-32793; RRID:AB_628036
Mouse monoclonal anti-TKT	Santa Cruz Biotechnology	Cat #sc-390179; RRID:AB_2925185
Mouse monoclonal anti-PRPS1/2	Santa Cruz Biotechnology	Cat #sc-100822; RRID:AB_2268859
Mouse monoclonal anti-Puromycin	Sigma-Aldrich	Cat #MABE343; RRID:AB_2566826
Rabbit recombinant monoclonal anti-GAPDH	Cell Signaling Technology	Cat #5174; RRID:AB_10622025
Rabbit polyclonal anti-PRPS1	Proteintech Group	Cat #15549-I-AP; RRID:AB_10694269
Rabbit polyclonal anti-PRPS2	Sigma-Aldrich	Cat #SAB2107995
Rabbit monoclonal anti-CAD	Cell Signaling Technology	Cat #93925; RRID:AB_2750933
Mouse monoclonal anti-PRPSAP1	Santa Cruz Biotechnology	Cat #sc-398422
Rabbit polyclonal anti-PRPSAP2	Proteintech Group	Cat #17814-1-AP; RRID:AB_10598314
Mouse monoclonal anti-TCP1-η	Santa Cruz Biotechnology	Cat #sc-271951; RRID:AB_10709576
Mouse monoclonal anti-AK2	Santa Cruz Biotechnology	Cat #sc-374095; RRID:AB_10915589
Alpaca monoclonal anti-ALFA HRP	Nanotag Biotechnologies	Cat #N1505-HRP; RRID:AB_3075989
Rabbit recombinant monoclonal anti-CTPS	Abcam	Cat #ab133743
Mouse monoclonal anti-UMPS	Santa Cruz Biotechnology	Cat #sc-398086; RRID:AB_2750932
Rabbit recombinant monoclonal anti-HPRT	Abcam	Cat #ab109021; RRID:AB_10866312
Rabbit recombinant anti-α-Tubulin	Abcam	Cat #ab176560; RRID:AB_2860019

(*continued on next page*)

(*continued*)

	SOURCE	IDENTIFIER
Rabbit polyclonal anti-AHCY	Sigma-Aldrich	Cat #HPA041225; RRID:AB_2677371
Mouse monoclonal anti-RPS7	Santa Cruz Biotechnology	Cat #sc-377317
Rabbit monoclonal anti-RPL11	Cell Signaling Technology	Cat #18163; RRID:AB_2798794
Rabbit monoclonal anti-eIF2α (phospho-Ser51)	Cell Signaling Technology	Cat #3398; RRID:AB_2096481
Rabbit recombinant monoclonal anti-eIF2α	Cell Signaling Technology	Cat #5324; RRID:AB_10692650
Rabbit polyclonal anti-H6PD	GeneTex	Cat #GTX101500; RRID:AB_1950476
Rabbit polyclonal anti-SOD2	Proteintech Group	Cat #24127-1-AP; RRID:AB_2879437
Rabbit monoclonal anti-Trx-1	Cell Signaling Technology	Cat #2429; RRID:AB_2272594
Rabbit recombinant monoclonal anti-Ki67	Abcam	Cat #ab16667; RRID:AB_302459
Rabbit monoclonal anti-Cyclin D2	Cell Signaling Technology	Cat #3741; RRID:AB_2070685
Rabbit polyclonal anti-Cyclin E1	Proteintech Group	Cat #11554-1-AP; RRID:AB_2071066
Rabbit recombinant monoclonal anti-Rb (phospho-Ser807/811)	Cell Signaling Technology	Cat #8516; RRID:AB_11178658
Mouse monoclonal anti-Rb	Cell Signaling Technology	Cat #9309; RRID:AB_823629
Rabbit polyclonal anti-Histone H3 (phospho-Ser10)	Cell Signaling Technology	Cat #9701; RRID:AB_331535
Rabbit monoclonal anti-Histone H3	Abcam	Cat #ab176842; RRID:AB_2493104
Mouse monoclonal anti-p21	Santa Cruz Biotechnology	Cat #sc-6246; RRID:AB_628073
Rabbit monoclonal anti-p27 Kip1	Cell Signaling Technology	Cat #3688; RRID:AB_2077836
Rabbit monoclonal anti-Bim	Cell Signaling Technology	Cat #2933 RRID:AB_1030947
Rabbit monoclonal anti-SQSTM1/p62	Cell Signaling Technology	Cat #39749; RRID:AB_2799160
Mouse monoclonal anti-Trx-2	Santa Cruz Biotechnology	Cat #sc-133201; RRID:AB_2145787
Rabbit monoclonal anti-Catalase	Cell Signaling Technology	Cat #14097; RRID:AB_2798391
Rabbit monoclonal anti-XO	Abcam	Cat #ab109235; RRID:AB_10863199
Mouse monoclonal anti-NNT	Santa Cruz Biotechnology	Cat#sc-390236
Rabbit monoclonal anti-Prdx1	Cell Signaling Technology	Cat #8499; RRID:AB_10950824
Rabbit monoclonal anti-LDHA	Cell Signaling Technology	Cat #3582; RRID:AB_2066887
Rabbit monoclonal anti-GCLM	Abcam	Cat #ab126704; RRID:AB_11127439
Rabbit polyclonal anti-GMPR2	Thermo Fisher Scientific	Cat #PA5-67012; RRID:AB_2665043
Rabbit polyclonal anti-NDUFA5	Proteintech Group	Cat #16640-1-AP; RRID:AB_2251270
Rabbit polyclonal anti-DAP13/NDUFA12	Proteintech Group	Cat #15793-1-AP; RRID:AB_2150475
Rabbit polyclonal anti-NDUFAF2	Proteintech Group	Cat #13891-1-AP; RRID:AB_10597105
Rabbit polyclonal anti-NDUFAF4	Proteintech Group	Cat #26003-1-AP; RRID:AB_2880329
Rabbit polyclonal anti-NDUFB5	Cusabio	Cat #CSB-PA015652ESR1HU
Rabbit polyclonal anti-NDUFS1	Cell Signaling Technology	Cat #60153; RRID:AB_2920533
Rabbit polyclonal anti-NDUFS2	GeneTex	Cat #GTX114924; RRID:AB_10624594
Rabbit polyclonal anti-NDUFS3	Proteintech Group	Cat #15066-1-AP; RRID:AB_2151109
Rabbit polyclonal anti-NDUFS4	GeneTex	Cat #GTX105662; RRID:AB_1950983
Rabbit polyclonal anti-NDUFS6	Proteintech Group	Cat #14417-1-AP; RRID:AB_2149024
Rabbit polyclonal anti-NDUFV2	Proteintech Group	Cat #15301-1-AP; RRID:AB_2149048
Mouse monoclonal anti-MTCO1	Abcam	Cat #ab14705; RRID:AB_2084810
Rabbit monoclonal anti-AMPKα (phospho-Thr172)	Cell Signaling Technology	Cat #2535; RRID:AB_331250

(*continued on next page*)

(*continued*)

	SOURCE	IDENTIFIER
Rabbit polyclonal anti-AMPKα	Cell Signaling Technology	Cat #2532; RRID:AB_330331
Rabbit polyclonal anti-IDH1	Cell Signaling Technology	Cat #3997; RRID:AB_1904011
Mouse monoclonal anti-IDH2	Cell Signaling Technology	Cat #60322
Mouse monoclonal anti-MDH2	Santa Cruz Biotechnology	Cat #sc-293474
Mouse monoclonal anti-HMGCR	Santa Cruz Biotechnology	Cat #sc-271595; RRID:AB_10650274
Rabbit monoclonal anti-NRF1	Cell Signaling Technology	Cat #46743; RRID:AB_2732888
Rabbit monoclonal anti-TrxR1	Cell Signaling Technology	Cat #15140; RRID:AB_2798725
Mouse monoclonal anti-TrxR2	Santa Cruz Biotechnology	Cat #sc-365714; RRID:AB_10844488
Rabbit polyclonal anti-GLRX	Proteintech Group	Cat #15804-1-AP; RRID:AB_11232210
Rabbit polyclonal anti-GLRX2	Proteintech Group	Cat #13381-1-AP; RRID:AB_10643373
Mouse monoclonal anti-GSR	Santa Cruz Biotechnology	Cat #sc-133245; RRID:AB_2295121
Rabbit monoclonal anti-Bak	Cell Signaling Technology	Cat #12105; RRID:AB_2716685
Rabbit monoclonal anti-Bax	Cell Signaling Technology	Cat #5023; RRID:AB_10557411
Rabbit polyclonal anti-Cleaved Caspase-3	Cell Signaling Technology	Cat #9661; RRID:AB_2341188
Rabbit monoclonal anti-FASN	Cell Signaling Technology	Cat #3180; RRID:AB_2100796
Mouse monoclonal anti-FLC	Santa Cruz Biotechnology	Cat #sc-390558
Rabbit polyclonal anti-NDUFB7	Proteintech Group	Cat #14912-1-AP; RRID:AB_2235903
Rabbit recombinant monoclonal anti-NDUFB9	Abcam	Cat #ab200198; RRID:AB_3668935
Rabbit polyclonal anti-ECSIT	Sigma-Aldrich	Cat #HPA042979; RRID:AB_10964063
Rabbit recombinant monoclonal anti-IMPDH1	Abcam	Cat #ab137112
Rabbit monoclonal anti-IMPDH2	Abcam	Cat #ab131158; RRID:AB_11156264
Rabbit polyclonal anti-MDH1	Proteintech Group	Cat #15904-1-AP; RRID:AB_2143279
Rabbit monoclonal anti-MTHFD1L	Cell Signaling Technology	Cat #14999; RRID:AB_2798681
Mouse monoclonal anti-SAMHD1	OriGene	Cat #TA502157S; RRID:AB_2622359
Rabbit monoclonal anti-SHMT1	Cell Signaling Technology	Cat #80715; RRID:AB_2799957
Rabbit polyclonal anti-SHMT2	Cell Signaling Technology	Cat #12762; RRID:AB_2798018
Mouse monoclonal anti-3PGDH	Santa Cruz Biotechnology	Cat #sc-100317; RRID:AB_2165393
Rabbit monoclonal anti-DHFR	Abcam	Cat #ab124814; RRID:AB_10975115
Mouse monoclonal anti-DYKDDDDK (FLAG) Tag	Cell Signaling Technology	Cat #8146; RRID:AB_10950495
Anti-mouse secondary antibody	Jackson ImmunoResearch	Cat #115-035-003; RRID:AB_10015289
Anti-rabbit secondary antibody	Jackson ImmunoResearch	Cat #111-035-003; RRID:AB_2313567
Bacterial and virus strains		
NEB Stable Competent *E. coli*	NEB	#C3040
Biological samples		
Chemicals, peptides, and recombinant proteins		
DMEM	Corning	Cat #10-013-CV
RPMI 1640	Corning	Cat #10-041-CV
Seahorse XF RPMI	Agilent	Cat #103576-100
Seahorse XF Glucose	Agilent	Cat #103577-100
Seahorse XF Glutamine	Agilent	Cat #103579-100
Seahorse XF Pyruvate	Agilent	Cat #103578-100
Seahorse XF Calibrant Solution	Agilent	Cat #100840-000
Fetal Bovine Serum (FBS)	Gibco	Cat #A5256701
Penicillin Streptomycin	Gibco	Cat #15140-122
Tetracycline	Selleckchem	Cat #S4490
Lipopolysaccharides (LPS)	Invitrogen	Cat #00-4976-03
Poly-d-lysine	Gibco	Cat #A3890401
PolyFect	QIAGEN	Cat #301105
Polybrene	Sigma-Aldrich	Cat #TR-1003
Retro-X Retroviral Concentrator	Takara Bio	Cat #631456
Lenti-X Lentiviral Concentrator	Takara Bio	Cat #631232
Puromycin	Gibco	Cat #A11138-03

(*continued on next page*)

(*continued*)

	SOURCE	IDENTIFIER
Blasticidin S HCl	Gibco	Cat #A11139-03
Doxycycline HCl	Sigma-Aldrich	Cat #D3447
RIPA Buffer	Thermo Fisher Scientific	Cat #89901
CHAPS Detergent	Millipore	Cat #75621-03-3
Red Blood Cell (RBC) Lysis Buffer	BioLegend	Cat #420301
TRIzol Reagent	Invitrogen	Cat #15596018
PEG-PCMal	Dojindo	Cat #SB20
Digitonin	Sigma-Aldrich	Cat #D141
Halt Protease and Phosphatase Inhibitor Cocktail	Thermo Fisher Scientific	Cat #78446
Benzonase Endonuclease	Millipore	Cat #E1014
Pierce BCA Protein Assay Kit	Thermo Fisher Scientific	Cat #23227
10X Tris/Glycine/SDS Running Buffer	Thermo Fisher Scientific	Cat #28362
10 % TGX Fastcast Gels	Bio-Rad	Cat #1610173
Trans-Blot Turbo PVDF Transfer Packs	Bio-Rad	Cat #1704156
Tween 20	Thermo Scientific Chemicals	Cat #J20605.AP
Albumin, Bovine, Fraction V (BSA)	Thermo Scientific Chemicals	Cat #J64100.22
Stripping Buffer	Thermo Fisher Scientific	Cat #46430
Propidium Iodide	Sigma-Aldrich	Cat #P4864
Trypan Blue	Sigma-Aldrich	Cat #T8154
RNase	Roche	Cat #111119915001
AgeI-HF Restriction Enzyme	NEB	Cat #R3552
EcoRI-HF Restriction Enzyme	NEB	Cat #R3101
SalI-HF Restriction Enzyme	NEB	Cat #R3138
BfuAI Restriction Enzyme	NEB	Cat #R0701
SuperSignal West Pico PLUS	Thermo Fisher Scientific	Cat #34580
SuperSignal West Dura	Thermo Fisher Scientific	Cat #34075
SuperSignal West Femto	Thermo Fisher Scientific	Cat #34095
SuperSignal West Atto	Thermo Fisher Scientific	Cat #A38555
AlamarBlue Reagent	Thermo Fisher Scientific	Cat #DAL1100
MitoSOX Red Superoxide Indicator	Thermo Fisher Scientific	Cat #M36008
CM-H_2DCFDA	Thermo Fisher Scientific	Cat #C6827
MitoTracker Green	Thermo Fisher Scientific	Cat #M7514
ER Tracker Red	Thermo Fisher Scientific	Cat #E34250
2-NBDG	Thermo Fisher Scientific	Cat #N13195
LysoTracker Green	Thermo Fisher Scientific	#L7526
FerroOrange	Dojindo	Cat #F374-10
BODIPY 581/591 C11	Thermo Fisher Scientific	Cat #D3861
All compounds used in dose-response experiments (Fig. 5A)	See Supplementary Table 1	See Supplementary Table 1
Critical commercial assays		
Seahorse XF Cell Mito Stress Test	Agilent	Cat #103015-100
Site-Directed Mutagenesis Kit	NEB	Cat #E0554S
Hi-Fi DNA Assembly Cloning Kit	NEB	Cat #E5520S
Gibson Assembly Cloning Kit	NEB	Cat #E5510S
GeneJET Plasmid MiniPrep Kit	Thermo Scientific	Cat #K0503
Murine Splenic B-cell Isolation Kit	Miltenyi Biotec	Cat #130-090-862
NEBNext Ultra II Directional RNA Library Prep Kit	NEB	Cat #E7760
NAD+/NADH-Glo Assay	Promega	Cat #G9072
NADP+/NADPH-Glo Assay	Promega	Cat #G9082
GSH/GSSG-Glo Assay	Promega	Cat #V6612
PureLink RNA Mini Kit	Thermo Scientific	Cat #12183018A
Qubit RNA BR Assay Kit	Thermo Scientific	Cat #Q10210
Gel Filtration Cal Kit Low Molecular Weight	Cytiva	Cat #28-4038-41
Gel Filtration Cal Kit High Molecular Weight	Cytiva	Cat #28-4038-42
Gel Filtration Markers Kit	Sigma-Aldrich	Cat #MWGF200
OxyBlot Protein Oxidation Detection Kit	Sigma-Aldrich	Cat #S7150
Deposited data		
Raw and processed RNA sequencing data	This paper	https://www.ncbi.nlm.nih.gov/geo/query/acc.cgi?acc=GSE282435
Experimental models: Cell lines		
Human: HEK293T	ATCC	Cat #CRL-3216; RRID:CVCL_0063
Human: CA46	ATCC	Cat #CRL-1648; RRID:CVCL_1101
Human: DG-75	ATCC	Cat #CRL-2625; RRID:CVCL_0244
Human: P493-6	Sigma-Aldrich	Cat #SCC279; RRID:CVCL_6783
Experimental models: Organisms/strains		
C57BL/6J (WT) mice strain	The Jackson Laboratory	Cat #000664 RRID:IMSR_JAX:000664
C57BL/6J-Tg(IghMyc)22Bri/J (Eμ-Myc) mice strain	Adams et al. [19]	Cat #002728 RRID:IMSR_JAX:002728
PRPS2 KO mice strain	Cunningham et al. [33]	Cunningham et al. [33]
Oligonucleotides		
Sequences for shRNA, CRISPR/Cas9 gRNA, site-directed mutagenesis and PCR primers	This paper	See Supplementary Table 2

(*continued on next page*)

(*continued*)

	SOURCE	IDENTIFIER
Recombinant DNA		
Prps1 cDNA	Horizon Discovery (Dharmacon)	Cat #MMM1013-202859297
Prps2 cDNA	Cunningham et al. [33]	Cunningham et al. [33]
pLKO.1_puro	Stewart et al. [66]	Addgene #8453; RRID:Addgene_8453
pMSCV_PIG	Mayr et al. [67]	Addgene #21654; RRID:Addgene_21654
pWZL_blast_myc	Boehm et al. [68]	Addgene #10674; RRID:Addgene_10674
FUGW	Lois et al. [69]	Addgene #14883; RRID:Addgene_14883
FUGW_blasticidin	This paper	N/A
FUGW_PRPS1-ALFA	This paper	N/A
FUGW_PRPS2-ALFA	This paper	N/A
FUGW_PRPS1(D52H)-ALFA	This paper	N/A
FUGW_PRPS1(A87T)-ALFA	This paper	N/A
FUGW_PRPS1(H193L)-ALFA	This paper	N/A
FUGW_PRPS2(E39A)-ALFA	This paper	N/A
pUC57_TPNOX	Cracan et al. [38]	Addgene #87853; RRID:Addgene_87853
pUC57_mitoTPNOX	Cracan et al. [38]	Addgene #87854; RRID:Addgene_87854
FUGW_TPNOX-FLAG	This paper	N/A
FUGW_mitoTPNOX-FLAG	This paper	N/A
pCW57.1_AOX-FLAG	Spinelli et al. [70]	Addgene #177984; RRID:Addgene_177984
PMXS_NDI1	Birsoy et al. [71]	Addgene #72876; RRID:Addgene_72876
psPAX2	Addgene	Addgene #12260; RRID:Addgene_12260
pMD2.G	Addgene	Addgene #12259; RRID:Addgene_12259
pUMVC	Stewart et al. [66]	Addgene #8449; RRID:Addgene_8449
pLKO.1_TRC cloning vector	Moffat et al. [72]	Addgene #10878; RRID:Addgene_10879
hCas9_D10A	Mali et al. [73]	Addgene #41816; RRID:Addgene_41816
Software and algorithms		
DESeq2 (v1.46.0)	Illumina	https://bioconductor.org/packages/release/bioc/html/DESeq2.html; RRID: SCR_015687
ggplot2 (v3.5.1)	R (v.4.3.3)	https://cran.r-project.org/web/packages/ggplot2/index.html; RRID:SCR_014601
Image Lab Software (v5.2.1)	Bio-Rad	https://www.bio-rad.com/en-us/product/image-lab-software?ID=KRE6P5E8Z; RRID:SCR_014210
FlowJo (v10)	BD Biosciences	https://www.flowjo.com; RRID:SCR_008520
GraphPad Prism 8	GraphPad	https://www.graphpad.com; RRID:SCR_002798
Seahorse Wave	Agilent	http://www.agilent.com/en-us/products/cell-analysis-(seahorse)/software-download-for-wave-desktop; RRID:SCR_014526
Adobe Illustrator (v27.9.1)	Adobe	http://www.adobe.com/products/illustrator.html; RRID:SCR_010279
MARS Data Analysis Software	BMG Labtech	https://www.bmglabtech.com/mars-data-analysis-software/; RRID:SCR_021015
Other		
Neon Transfection Instrument	Invitrogen	Cat #MPK5000
Trans-Blot Turbo Transfer System	Bio-Rad	Cat #1704150; RRID:SCR_023156
Seahorse XFe96 Analyzer	Agilent	RRID:SCR_019545
Seahorse XFe96 Cell Culture Microplates	Agilent	Cat #103799-100
Seahorse XFe96 FluxPak	Agilent	Cat #103792-100
FACSAria III Cell Sorter	BD Biosciences	RRID:SCR_016695
LSRFortessa Cell Analyzer	BD Biosciences	Cat #649225; RRID:SCR_018655
CLARIOstar Microplate Reader	BMG Labtech	RRID:SCR_026330
ChemiDoc Touch Imaging System	Bio-Rad	Cat #12003153; RRID:SCR_021693
Vanquish UHPLC	Thermo Fisher Scientific	RRID:SCR_025713
RNA 2100 Bioanalyzer Instrument	Agilent	RRID:SCR_018043
NextSeq 550 RNA Sequencer	Illumina	RRID:SCR_016381
Qubit 4 Fluorometer	Invitrogen	N/A
Superose 6 Increase 3.2/300 Column	Cytiva	Cat #29-0915-98
3K MWCO Filter	Thermo Fisher Scientific	Cat #88512
Countess II FL	Invitrogen	RRID:SCR_025370

Experimental model details

Mice

C57BL/6 (WT) mice (The Jackson Laboratory #000664) and C57BL/6J-Tg(IghMyc)22Bri/J (Eμ-Myc) mice [19] (The Jackson Laboratory #002728) were obtained from The Jackson Laboratory. PRPS2 KO mouse strain [33] used for this research project was created from ES cell clone PRPS2$^{tm1a(KOMP)Wtsi}$ (EPD0110_2_A05), obtained from KOMP Repository (www.komp.org) and generated by the Wellcome Trust Sanger Institute.

Mice were generated at the Transgenic Animal and Genome Editing (TAGE) core at Cincinnati Children's Hospital Medical Center (CCHMC). Male mice (6w) were used to collect the data included in this study. All procedures were performed in compliance with ARRIVE guidelines and carried out in accordance with the National Research Council's Guide for the Care and Use of Laboratory Animals and the protocols approved by the Institutional Animal Care and Use Committee under protocol no. 21-04-16-02.

Cell culture

CA46 (ATCC #CRL-1648; male, human, Burkitt's lymphoma), DG-75 (ATCC #CRL-2625; male, human, Burkitt's lymphoma), and P493-6 (Sigma-Aldrich #SCC279; sex unspecified, human, lymphoblastoid) cells were cultured in complete RPMI 1640 medium (Corning #10-041-CV) supplemented with 10 % (v/v) fetal bovine serum (FBS) (Gibco #A5670701) and 1 % (v/v) penicillin/streptomycin (Gibco #15140–122). P493-6 cells were cultured in the presence of 0.1 μg/mL tetracycline (Selleckchem #S4490) for 48 h s to achieve *c-Myc* suppression. For experiments involving the expression of Alternative Oxidase (AOX), cells were treated with 0.1 μg/mL doxycycline (Sigma-Aldrich #D3447) for 24 h s to induce expression. HEK293T cells (ATCC #CRL-3216; female, human, embryonic kidney epithelial-like) used for virus production were cultured in complete DMEM medium (Corning #10-013-CV) supplemented with 10 % (v/v) FBS and 1 % (v/v) penicillin/streptomycin. Cell lines tested negative for mycoplasma contamination after receipt from ATCC. All cells were cultured at 37 °C in a 5 % CO_2 incubator.

Method details

Plasmid generation

Lentiviral expression plasmids for shRNA-mediated knockdown were derived, as follows. shRNA sequences targeting *PRPS1* and *PRPS2* as well as a non-targeting control sequence (see Table S2) were annealed and subsequently ligated into the pLKO.1_puro cloning vector (Addgene #8453 [61]) via restriction cloning, using AgeI and EcoRI restriction sites. Lentiviral expression plasmids for ALFA-tagged peptides were derived, as follows. *Prps1* cDNA (Horizon Discovery #MMM1013-202859297) and *Prps2* cDNA (previously described [33]) were subcloned into the pMSCV_PIG cloning vector (Addgene #21654 [62]) using the SalI and EcoRI restriction sites. The blasticidin expression cassette from pWZL_Blast_myc (Addgene #10674 [63]) was subcloned into FUGW (Addgene #14883 [64]) to replace bleomycin. The cDNAs encoding *PRPS1* and *PRPS2* were PCR amplified from the pMSCV_PIG vector and ligated with the PCR-amplified FUGW_blasticidin backbone using Gibson assembly. Sequences encoding the ALFA epitope tag were engineered in the primers to C-terminally tag the proteins (FUGW_PRPS1-ALFA, FUGW_PRPS2-ALFA). Site-directed mutagenesis (SDM) was performed to introduce point mutations into FUGW_PRPS1-ALFA and FUGW_PRPS2-ALFA. To accomplish this, template DNA was mixed with complementary primers containing the appropriate base substitutions for the target gene (see Table S2) along with Q5 Hot Start Hi-Fi 2X MM (NEB #M0494), and the mixture was PCR amplified according to manufacturer's protocol. KLD treatment was then performed on the PCR product using 10X KLD enzyme mix (NEB #M0554) and 2X KLD reaction buffer (NEB #B0554) to circularize the mutated plasmid. DNA product was then transformed using 5-alpha Competent *E. coli* cells (NEB #C3040), and subsequently isolated via GeneJET Plasmid MiniPrep Kit (Thermo Scientific #K0503), according to manufacturer's protocol. Sanger sequencing was performed to confirm incorporation of mutation [FUGW_PRPS1(D52H)-ALFA, FUGW_PRPS1(A87T)-ALFA, FUGW_PRPS1(H193L)-ALFA, FUGW_PRPS2(E39A)-ALFA]. Lentiviral expression plasmids for TPNOX and mitoTPNOX were derived, as follows. *TPNOX* (Addgene #87853 [38]) and *mitoTPNOX* (Addgene #87854 [38]) cDNA were amplified with primers to include the C-terminal FLAG epitope tag of each plasmid vector and subsequently cloned into the aforementioned FUGW_blasticidin plasmid assembly via restriction digest using AgeI and EcoRI restriction sites (FUGW_TPNOX-FLAG, FUGW_mitoTPNOX-FLAG). Lentiviral expression plasmid for doxycycline-inducible mammalian AOX expression was obtained from Addgene (Addgene #177984 [65]). Retroviral expression plasmid for mammalian NDI1 expression was obtained from Addgene (Addgene #72876 [66]).

Virus production and transduction

Lentivirus was produced in HEK293T cells by co-transfecting the lentiviral transfer vector with psPAX2 (Addgene #12260) and pMD2.G (Addgene #12259). Retrovirus was produced in HEK293T cells by co-transfecting the retroviral transfer vector with pUMVC (Addgene #8449 [61]) and pMD2.G. Transfection was carried out using PolyFect transfection reagent (QIAGEN #301105), and the media was replaced after 24 h. Viral supernatant was collected at 48 h and 72 h post-transfection, filtered (45 μm), and concentrated using Lenti-X (Takara Bio #631232) or Retro-X (Takara Bio #631456) concentrators.

Viral transduction of suspension cell culture was achieved via spinfection, as follows. 3×10^6 cells were collected, per transduction, and resuspended in 1 mL of filtered and concentrated viral media containing 8 μg/mL polybrene (Sigma-Aldrich #TR-1003) to enhance transduction efficiency. Viral cell suspensions were centrifuged in 24-well plates at 200×*g* for 1hr, before subsequent incubation at 37 °C. Complete media was added to the viral media (1:1) overnight, and the process was repeated 1–2X in consecutive days. After final spinfection was completed, cells were left to recover in complete media for 24 h s prior to the addition of the appropriate selection media.

CRISPR-Cas9 Genome Editing

PRPS1 and *PRPS2* knockouts in CA46 and DG-75 cell lines were achieved using a CRISPR-Cas9 nickase system, as follows. BfuAI restriction sites, tracrRNA, and a GFP tag were inserted into the pLKO.1_TRC cloning vector (Addgene #10878 [67]). Complementary PRPS1 and PRPS2 crRNA oligonucleotides were generated for both the top (+) and bottom (−) strands (see Table S2) of the respective target gene to facilitate Cas9 D10A-mediated nickase activity. Annealed crRNA oligonucleotide strands were inserted into the BfuAI-digested pLKO.1_TRC backbone. The (+) sgRNA and (−) sgRNA pLKO plasmids were then electroporated with hCas9_D10A (Addgene #41816 [68]) at a 1:1:1 ratio via the Invitrogen Neon Transfection System, according to manufacturer's protocols. After 48 h, cells were single-cell sorted into individual wells of a 96-well plate based on GFP expression, via BD FACSAria III. Single cells were subject to clonal expansion until sufficient material was able to be gathered for thorough knockout validation via Western Blotting, PCR, and DNA sequencing.

SDS-PAGE and western blotting

For denaturing cell lysis, cells were first washed 1X with ice-cold PBS (Corning #21-040-CV) and subsequently lysed using RIPA buffer (Thermo Fisher Scientific #89901) supplemented with 1X protease and phosphatase inhibitor cocktail (Thermo Fisher Scientific #78446). Cleared protein lysates were quantified using BCA reagent (Thermo Fisher Scientific #23227), and subsequently combined with 1X Laemmeli sample buffer prior to separation on 10 % TGX Fastcast gels (Bio-Rad #1610173) in 1X Tris/Glycine/SDS running buffer (Thermo Fisher Scientific #28362) at 120V for ~1hr. Separated proteins were then transferred onto 0.2 μm PVDF membranes (Bio-Rad #1704156) using the Bio-Rad Trans-Blot Turbo Transfer system. PVDF membranes were subsequently blocked for 1hr at room temperature (RT) with 5 % (w/v) milk in Tris-Buffered Saline containing 0.1 % Tween-20 (Thermo Scientific Chemicals #J20605.AP) (TBS-T). After blocking, the membranes were washed (3X in TBS-T) and incubated overnight at 4 °C with primary antibodies (diluted 1:1000) prepared in 3 % BSA (Thermo Scientific Chemicals #J64100.22) in TBS-T. Membranes were again washed (3X in TBS-T) and incubated at RT with corresponding secondary antibodies from Jackson ImmunoResearch (diluted 1:25000) in 5 % (w/v) milk in TBS-T. Blots were visualized using chemiluminescent substrates from Thermo Fisher Scientific via the Bio-Rad ChemiDoc Touch Imaging System. To facilitate re-probing, Restore PLUS Western Blot Stripping Buffer (Thermo Fisher Scientific #46430) was used to strip the blots after imaging.

To determine oxidative state of proteins, cells were first washed 1X with ice cold PBS and subsequently incubated in 1 % CHAPS detergent (Millipore #75621-03-3) containing 1 mmol/L PEG-PCMal (Dojindo #SB20) for 30 min at 37 °C. Cleared protein lysates were quantified using BCA reagent and subsequently resolved via SDS-PAGE in non-reducing conditions (DTT-free 1X Laemmeli sample buffer, no boil).

All primary and secondary antibodies used in this study are listed in the Key Resource Table.

Murine splenic primary B lymphocyte isolation

Post-euthanasia (CO_2 asphyxiation followed by cervical dislocation), spleens of each mouse (male, 6w) were dissected and immediately stored in ice-cold 1X PBS. Scalpel was used to break through the integrity of the spleen casing, prior to filtration through 40 μm cell strainers (Corning #431750) using a 1 mL syringe plunger and 1X PBS. Cell suspension was then centrifuged at 300×*g* for 5min, before the supernatant was discarded and pelleted cells were resuspended in 5 mL 1X red blood cell (RBC) lysis buffer (BioLegend #420301), according to manufacturer's protocol. Cell suspension was again centrifuged at 300×*g* for 5 min, repeating the RBC lysis process until cell pellets were homogenously white in color. 10 mL PBS was added to neutralize the lysis buffer, and cell suspension was again centrifuged at 300×*g* for 5min. Cell pellets were resuspended in 1X PBS, counted using Trypan blue (Sigma-Aldrich #T8154) at 1/10 dilution via Countess II FL, and then prepared for B-cell isolation via negative selection (Miltenyi Biotec #130-090-862), according to manufacturer's protocol. To induce B-cell activation, lipopolysaccharides (LPS, Invitrogen #00-4976-03) were added to complete RPMI 1640 media at a 1X concentration (5 μg/mL) immediately following isolation.

RNA sequencing

Following murine splenic primary B lymphocyte isolation, RNA was obtained using TRIzol reagent (Invitrogen #15596018), according to manufacturer's protocol. RNA samples were processed by the University of Cincinnati Department of Environmental and Public Health Sciences Genomics, Epigenomics and Sequencing Core. NEBNext Ultra II Directional RNA Library Prep Kit (NEB #E7760) was used for RNA-seq library preparation. Sample RNA passed through a quality control step using Agilent RNA 2100 Bioanalyzer and sequenced via PolyA RNA-seq (SR 1 × 85 bp, ~25 M reads, >20 M pass filter) on Illumina NextSeq 550 sequencer [69]. Differentially expressed genes (DEGs) analysis was performed using Illumina DEseq2 (v1.1.0), and volcano plots were generated using ggplot2 in R (v4.3.3). DEGs were selected by limiting the adjusted p-value <0.05. For Eμ-Myc vs WT mice (Fig. 1B), from the total of 15,430 genes analyzed, 3785 were significantly upregulated and 3749 were significantly downregulated. For Eμ-Myc; PRPS2 KO vs Eμ-Myc mice (Fig. 4A), from the total of 17,611 genes analyzed, 4 were significantly downregulated and none were significantly upregulated.

Oxygen consumption rate (OCR), extracellular acidification rate (ECAR)

Agilent Seahorse XF Cell Mito Stress Test (Agilent #103015–100) was used to measure OCR and ECAR in P493-6 cells that had been removed from tetracycline-containing media for indicated periods of time (0 h s, 2 h s, 16 h s, 24 h s). The day prior to the assay, Seahorse XFe96 Cell Culture Microplates (Agilent #103799–100) were coated in poly-d-lysine (Gibco #A3890401) according to manufacturer's protocol to ensure adherence of suspension cells. 10^5 cells were plated in 50 μL Seahorse XF RPMI media (Agilent #103576–100) [(supplemented with 1 mM pyruvate (Agilent #103578–100), 2 mM glutamine (Agilent #103579–100) and 10 mM glucose (Agilent #103577–100)] per replicate, based on previously determined optimal seeding density, and plates were centrifuged at 200×*g* for 1min to adhere cells. Cells were incubated at 37 °C in a non-CO_2 containing incubator for 30 min, prior to the addition of 130 μL complete Seahorse XF RPMI media. Cells were incubated once more for an additional 30 min prior to running the assay. 1hr prior to running the assay, H_2O added overnight to Seahorse XFe96 FluxPak sensor cartridge (Aglient #103792–100) was replaced with Seahorse XF Calibrant Solution (Agilent #100840–000) and incubated at 37 °C in a non-CO_2 containing incubator. Immediately prior to running the assay, sensor cartridge was loaded with compounds in the following orientation: 20 μL oligomycin (15 μM) to Port "A"; 22 μL FCCP (10 μM) to Port "B"; 25 μL rotenone + antimycin A (5 μM each) to Port "C", such that the final working concentrations of each compound were 1.5 μM, 1 μM and 500 nM, respectively. Injections were sequentially added in accordance with the Seahorse XF Cell Mito Stress Test using the Agilent XFe96 Seahorse Analyzer and data was analyzed via Agilent WAVE software.

AlamarBlue intracellular reduction assay

Cells were seeded in black-walled, clear-bottom 96-well plates at a density of 2.5×10^5 cells/well (CA46, DG-75, P493-6) or 5×10^5 cells/well (isolated splenic murine primary B lymphocytes) in 180 μL complete RPMI 1640 medium. 20 μL AlamarBlue reagent (Thermo Fisher Scientific #DAL1100) was added to each well to achieve a final concentration of 10 % (v/v), prior to incubation for 4 h s at 37 °C in a 5 % CO_2 incubator. Post-incubation, AlamarBlue fluorescence was measured via the BMG Labtech CLARIOStar microplate reader, with ex/em of 560nm/590 nm, respectively. Data was collected via MARS Data Analysis Software, with background fluorescence subtracted from all experimental wells. For drug treatment assays involving P493-6 cells, cells were treated for 48 h s prior to assay at the following concentrations: vehicle control (DMSO)(1 % v/v), chloramphenicol (100 μM), G6PDi-1 (10 μM), allopurinol (100 μM) and brequinar (100 μM) (see Table S1).

Fluorescent dyes

For each fluorescent dye used, 1.5 × 10^6 cells were collected per replicate, in triplicate. Cell suspensions were centrifuged and washed with 1X PBS prior to incubation with the respective dye, with the working concentration and incubation time for each dye as follows: MitoSOX Red Superoxide Indicator (Thermo Fisher Scientific #M36008)(100 nM, 30 min), CM-H_2DCFDA (Thermo Fisher Scientific #C6827)(500 nM, 30 min), MitoTracker Green (Thermo Fisher Scientific #M7514)(100 nM, 30 min), ER Tracker Red (Thermo Fisher Scientific #E34250)(1 μM, 30 min), 2-NBDG (Thermo Fisher Scientific #N13195)(100 μM, 15 min), LysoTracker Green (Thermo Fisher Scientific #L7526)(50 nM, 30 min), FerroOrange (Dojindo #F374-10)(1 μmol/L, 30 min), BODIPY 581/591 C11 (Thermo Fisher Scientific #D3861)(5 μM, 30 min). After incubation, cell suspensions were collected, centrifuged and washed with 1X PBS. Cells were again centrifuged and resuspended in FACS buffer (2.5 % FBS in PBS) on ice for subsequent analysis via BD LSRFortessa.

Luciferase-based metabolite GLO assays

The following kits were utilized for luciferase-based GLO-assays and executed in accordance with manufacturer's protocols: NAD+/NADH-Glo Assay (Promega #G9072); NADP+/NADPH-Glo Assay (Promega #G9082); GSH/GSSG-Glo Assay (Promega #V6612). All absorbance measurements were obtained via BMG Labtech CLARIOStar microplate reader, and data was collected via MARS Data Analysis Software.

Per cell measurements

5 × 10^6 cells were collected per analysis (RNA, protein, cell size), in triplicate. Cells were collected, centrifuged and washed with 1X ice-cold PBS. Protein lysates were obtained from each cell line in accordance with SDS-PAGE/Western Blotting protocol, followed with subsequent quantification via BCA assay. RNA was isolated from cells via PureLink RNA Mini Kit (Thermo Scientific #12183018A), according to manufacturer's protocol. RNA concentration was obtained via Qubit 4 Fluorometer, using the Qubit RNA BR Assay Kit (Thermo Scientific #Q10210), according to manufacturer's protocol. Average cell size was obtained via Countess II FL, using Trypan blue staining at a 1:1 ratio.

Cell cycle analysis

For cell cycle analysis experiments, 5 × 10^5 cells were analyzed per replicate, in triplicate. Cells were centrifuged and washed with 1X ice-cold PBS, prior to fixation in 1.2 mL ice-cold 66 % ethanol in PBS with gentle vortexing. Cells were stored at 4° for at least 2 h (stable up to 4w) prior to centrifugation and subsequent washing with 1X PBS. Cells were again centrifuged, supernatant was discarded, and cells were resuspended in 200 μL PBS containing Propidium Iodide (Sigma-Aldrich #P4864) at a final concentration of 50 μg/mL and RNase (Roche #11119915001) at a final concentration of 50 μg/mL. Cells were incubated in the dark at 37 °C in a 5 % CO_2 incubator for 30 min prior to analysis via BD LSRFortessa.

Puromycylation assay

For each puromycylation assay, 1 × 10^6 cells were collected and plated in 6-well plates, per replicate. Puromycin (Gibco #A11138-03) was added at a working concentration of 10 μg/mL to each replicate for 30 min, before cells were collected and prepared in accordance with SDS-PAGE/Western Blotting protocol.

Size exclusion chromatography

Cells were lysed using non-denaturing lysis buffer [50 mM Tris-Cl, pH 7.5, 200 mM NaCl, 1 % digitonin, 1 mM TCEP (tris(2-carboxyethyl)phosphine), 1 mM MgCl2, benzonase and 1X protease and phosphatase inhibitor cocktail] for 20 min on ice. The cell lysates were then clarified by centrifugation at 15,000×*g* for 15 min at 4 °C and subsequently filtered using a 0.22 μm filter. ~200 μg of cell lysates were loaded onto a Superose 6 Increase 3.2/300 column (Cytiva #29-0915-98) at the flow rate of 0.04 mL/min using Thermo Vanquish UHPLC, using mobile phase (0.1 M Na_2HPO_4, 0.1 M NaCl, pH 7.5). After passing through the void volume, the sample fractions were collected and concentrated using a 3K MWCO filter (Thermo Fisher Scientific #88512) and analyzed via SDS-PAGE/Western Blotting. Gel filtration calibration kits (Cytiva #28-4038-41, Cytiva #28-4038-42, Sigma-Aldrich #MWGF200-1 KT) were used to monitor column performance over time. Different internal standards were probed for molecular weight calibration: CAD [70] [(GLN-dependent carbamoyl phosphate synthetase (CPS-2), aspartate transcarbamylase (ATC), dihydroorotase(DHO)], TCP-1η [71] (T-Complex Protein 1 subunit eta), FASN (Fatty Acid Synthase) [72] and FLC (Ferritin Light Chain) [73] form complexes of around 1500 kDa, 900 kDa, 540 kDa and 480 kDa, respectively, while HK2 (Hexokinase 2) and AK2 (Adenylate Kinase 2) are mostly monomeric at 102 kDa and 26 kDa, respectively. The elution profile of PRPS complex components was compared with that of CAD, TCP-1η, FASN, FLC, HK2 and AK2, which were used as internal standards to estimate the size of the PRPS enzyme complex. Internal standards were probed in every SEC run.

Global protein oxidation

Global protein oxidation was determined via the OxyBlot Protein Oxidation Detection Kit (Sigma-Aldrich #S7150), according to manufacturer's protocol, and detected via SDS-PAGE/Western blotting.

Pharmacological dose-response screening

For each dose-response curve, cells were plated at a density of 6.5 × 10^4 in 180 μL of complete RPMI 1640 media in individual wells of a black-walled, clear-bottom 96-well plate with 4 blank wells containing media with no cells. 20 μL of AlamarBlue cell viability reagent was added to each well, such that the final AlamarBlue concentration was 10 % (v/v). Cells were left to incubate for 4 h s at 37 °C in a 5 % CO_2 incubator, prior to obtaining the initial 0hr reading using the BMG Labtech CLARIOStar microplate reader using ex/em of 560nm/590 nm, respectively. Stock concentrations of each compound (see Table S1) were prepared in increasing 100X increments, such that adding 2 μL of each stock would yield the final desired working concentration. After the initial 0hr reading, 2 μL of each prepared stock was added to each cell line, and subsequent microplate readings were obtained via the BMG Labtech CLARIOStar microplate reader at 24 h s, 48 h s, and 72 h s post-treatment. If sufficient concentrations were not used to yield a proper EC_{50} dose-response curve, the experiment was repeated with a more accurate range of concentrations (unless solubility of original stock concentration proved to be a limiting factor). All data was collected via the MARS Data Analysis Software.

Abbreviations

Dithiothreitol (DTT); extracellular acidification rate (ECAR); endoplasmic reticulum (ER); electron transport chain (ETC); reduced glutathione (GSH); glutathione reductase (GSR); oxidized glutathione (GSSG); knockout (KO); lipopolysaccharides (LPS); N-acetyl-L-cysteine (NAC); oxygen consumption rate (OCR); oxidative phosphorylation (OXPHOS); oxidative pentose phosphate pathway (oxPPP); phosphoribosyl pyrophosphate (PRPP); phosphoribosyl pyrophosphate synthetase (PRPS); reactive oxygen species (ROS); thioredoxin reductase (TRXR); wild-type (WT); xanthine oxidoreductase (XOR).

References

[1] C. Lourenco, et al., MYC protein interactors in gene transcription and cancer, Nat. Rev. Cancer 21 (2021) 579–591.

[2] S.K. Das, B.A. Lewis, D. Levens, MYC: a complex problem, Trends Cell Biol. 33 (2023) 235–246.

[3] K.I. Zeller, et al., Global mapping of c-Myc binding sites and target gene networks in human B cells, Proc. Natl. Acad. Sci. USA 103 (2006) 17834–17839.

[4] F.R. Dejure, M. Eilers, MYC and tumor metabolism: chicken and egg, EMBO J. 36 (2017) 3409–3420.

[5] Z.E. Stine, Z.E. Walton, B.J. Altman, A.L. Hsieh, C.V. Dang, MYC, metabolism, and cancer, Cancer Discov. 5 (2015) 1024–1039.

[6] N. Hay, Reprogramming glucose metabolism in cancer: can it be exploited for cancer therapy? Nat. Rev. Cancer 16 (2016) 635–649.

[7] Y.-C. Liu, et al., Global regulation of nucleotide biosynthetic genes by c-Myc, PLoS One 3 (2008) e2722.

[8] K.J. Campbell, R.J. White, MYC regulation of cell growth through control of transcription by RNA Polymerases I and III, Cold Spring Harb. Perspect. Med. 4 (2014) a018408 a018408.

[9] J. Van Riggelen, A. Yetil, D.W. Felsher, MYC as a regulator of ribosome biogenesis and protein synthesis, Nat. Rev. Cancer 10 (2010) 301–309.

[10] H. Ji, et al., Cell-type independent MYC target genes reveal a primordial signature involved in biomass accumulation, PLoS One 6 (2011) e26057.

[11] F. Morrish, D. Hockenbery, MYC and mitochondrial biogenesis, Cold Spring Harb. Perspect. Med. 4 (2014) a014225 a014225.

[12] G. Bretones, M.D. Delgado, J. León, Myc and cell cycle control, Biochim. Biophys. Acta, Gene Regul. Mech. 1849 (2015) 506–516.

[13] J.D. Hayes, A.T. Dinkova-Kostova, K.D. Tew, Oxidative stress in cancer, Cancer Cell 38 (2020) 167–197.

[14] J. Dan Dunn, L.A. Alvarez, X. Zhang, T. Soldati, Reactive oxygen species and mitochondria: a nexus of cellular homeostasis, Redox Biol. 6 (2015) 472–485.

[15] G. Donati, et al., Oxidative stress enhances the therapeutic action of a respiratory inhibitor in MYC-driven lymphoma, EMBO Mol. Med. 15 (2023) e16910.

[16] G. Donati, et al., Targeting mitochondrial respiration and the BCL2 family in high-grade MYC- associated B-cell lymphoma, Mol. Oncol. 16 (2022) 1132–1152.

[17] B. Perillo, et al., ROS in cancer therapy: the bright side of the moon, Exp. Mol. Med. 52 (2020) 192–203.

[18] Q. Cai, L.J. Medeiros, X. Xu, K.H. Young, *MYC*-driven aggressive B-cell lymphomas: biology, entity, differential diagnosis and clinical management, Oncotarget 6 (2015) 38591–38616.

[19] J.M. Adams, et al., The c-myc oncogene driven by immunoglobulin enhancers induces lymphoid malignancy in transgenic mice, Nature 318 (1985) 533–538.

[20] M. Schuhmacher, The transcriptional program of a human B cell line in response to Myc, Nucleic Acids Res. 29 (2001) 397–406.

[21] K. Singh, et al., c-MYC regulates mRNA translation efficiency and start-site selection in lymphoma, J. Exp. Med. 216 (2019) 1509–1524.

[22] L.S. Hart, et al., ER stress–mediated autophagy promotes Myc-dependent transformation and tumor growth, J. Clin. Investig. 122 (2012) 4621–4634.

[23] L. Baird, M. Yamamoto, The molecular mechanisms regulating the KEAP1-NRF2 pathway, Mol. Cell Biol. 40 (2020) e00099.

[24] L. Chen, et al., NADPH production by the oxidative pentose-phosphate pathway supports folate metabolism, Nat. Metab. 1 (2019) 404–415.

[25] A. D'Andrea, et al., The mitochondrial translation machinery as a therapeutic target in Myc- driven lymphomas, Oncotarget 7 (2016) 72415–72430.

[26] J.B. Hanson, W.A. Krueger, Impairment of oxidative phosphorylation by D-threo- and L- threo-chloramphenicol, Nature 211 (1966) 1322, 1322.

[27] J.M. Ghergurovich, et al., A small molecule G6PD inhibitor reveals immune dependence on pentose phosphate pathway, Nat. Chem. Biol. 16 (2020) 731–739.

[28] H. Ying, et al., Oncogenic Kras maintains pancreatic tumors through regulation of anabolic glucose metabolism, Cell 149 (2012) 656–670.

[29] K. Okamoto, T. Kusano, T. Nishino, Chemical nature and reaction mechanisms of the molybdenum cofactor of Xanthine Oxidoreductase, Curr. Pharm. Des. 19 (2013) 2606–2614.

[30] Z. Wu, et al., Electron transport chain inhibition increases cellular dependence on purine transport and salvage, Cell Metab. 36 (2024) 1504–1520, e9.

[31] I. Ben-Sahra, G. Hoxhaj, S.J.H. Ricoult, J.M. Asara, B.D. Manning, mTORC1 induces purine synthesis through control of the mitochondrial tetrahydrofolate cycle, Science 351 (2016) 728–733.

[32] J.M. Nosal, R.L. Switzer, M.A. Becker, Overexpression, purification, and characterization of recombinant human 5-phosphoribosyl-1-pyrophosphate synthetase isozymes I and II, J. Biol. Chem. 268 (1993) 10168–10175.

[33] J.T. Cunningham, M.V. Moreno, A. Lodi, S.M. Ronen, D. Ruggero, Protein and nucleotide biosynthesis are coupled by a single rate-limiting enzyme, PRPS2, to drive cancer, Cell 157 (2014) 1088–1103.

[34] B. Karki, et al., Evolutionary Origins and Innovations Sculpting the Mammalian PRPS Enzyme Complex, bioRxiv (Preprint), 2024, 2024.10.01.616059.

[35] S. Li, Y. Lu, B. Peng, J. Ding, Crystal structure of human phosphoribosylpyrophosphate synthetase 1 reveals a novel allosteric site, Biochem. J. 401 (2007) 39–47.

[36] B.B. Seo, et al., Molecular remedy of complex I defects: rotenone-insensitive internal NADH- quinone oxidoreductase of *Saccharomyces cerevisiae* mitochondria restores the NADH oxidase activity of complex I-deficient mammalian cells, Proc. Natl. Acad. Sci. USA 95 (1998) 9167–9171.

[37] G. Vanlerberghe, Alternative oxidase: a mitochondrial respiratory pathway to maintain metabolic and signaling homeostasis during abiotic and biotic stress in plants, Int. J. Mol. Sci. 14 (2013) 6805–6847.

[38] V. Cracan, D.V. Titov, H. Shen, Z. Grabarek, V.K. Mootha, A genetically encoded tool for manipulation of NADP+/NADPH in living cells, Nat. Chem. Biol. 13 (2017) 1088–1095.

[39] R.L. Switzer, D.C. Sogin, Regulation and mechanism of phosphoribosylpyrophosphate synthetase. V. Inhibition by end products and regulation by adenosine diphosphate, J. Biol. Chem. 248 (1973) 1063–1073.

[40] M.A. Becker, P.R. Smith, W. Taylor, R. Mustafi, R.L. Switzer, The genetic and functional basis of purine nucleotide feedback-resistant phosphoribosylpyrophosphate synthetase superactivity, J. Clin. Investig. 96 (1995) 2133–2141.

[41] P. García-Pavía, et al., Phosphoribosylpyrophosphate synthetase overactivity as a cause of uric acid overproduction in a young woman, Arthritis Rheum. 48 (2003) 2036–2041.

[42] X. Liu, et al., Loss-of-function mutations in the PRPS1 gene cause a type of nonsyndromic X-linked sensorineural deafness, DFN2, Am. J. Hum. Genet. 86 (2010) 65–71.

[43] G. Donati, B. Amati, MYC and therapy resistance in cancer: risks and opportunities, Mol. Oncol. 16 (2022) 3828–3854.

[44] J.C. Lukesh, M.J. Palte, R.T. Raines, A potent, versatile disulfide-reducing agent from aspartic acid, J. Am. Chem. Soc. 134 (2012) 4057–4059.

[45] G. Aldini, et al., N-Acetylcysteine as an antioxidant and disulphide breaking agent: the reasons why, Free Radic. Res. 52 (2018) 751–762.

[46] W. Xiao, J. Loscalzo, Metabolic responses to reductive stress, Antioxid. Redox Signal. 32 (2020) 1330–1347.

[47] K.P. Rice, P.G. Penketh, K. Shyam, A.C. Sartorelli, Differential inhibition of cellular glutathione reductase activity by isocyanates generated from the antitumor prodrugs Cloretazine and BCNU, Biochem. Pharmacol. 69 (2005) 1463–1472.

[48] C. Roder, M.J. Thomson, Auranofin: repurposing an old drug for a golden new age, Drugs R&D 15 (2015) 13–20.

[49] E.D. Hawkins, M.L. Turner, M.R. Dowling, C. Van Gend, P.D. Hodgkin, A model of immune regulation as a consequence of randomized lymphocyte division and death times, Proc. Natl. Acad. Sci. USA 104 (2007) 5032–5037.

[50] I.M. De Alboran, et al., Analysis of c-MYC function in normal cells via conditional gene- targeted mutation, Immunity 14 (2001) 45–55.

[51] D. Chen, et al., Coupled analysis of transcriptome and BCR mutations reveals role of OXPHOS in affinity maturation, Nat. Immunol. 22 (2021) 904–913.

[52] K.-J. Jang, et al., Mitochondrial function provides instructive signals for activation-induced B- cell fates, Nat. Commun. 6 (2015) 6750.

[53] A.M. Flinn, A.R. Gennery, Adenosine deaminase deficiency: a review, Orphanet J. Rare Dis. 13 (2018) 65.

[54] A.P.M. De Brouwer, et al., Arts syndrome is caused by loss-of-function mutations in PRPS1, Am. J. Hum. Genet. 81 (2007) 507–518.

[55] H.-J. Kim, et al., Mutations in PRPS1, which encodes the phosphoribosyl pyrophosphate synthetase enzyme critical for nucleotide biosynthesis, cause hereditary peripheral neuropathy with hearing loss and optic neuropathy (CMTX5), Am. J. Hum. Genet. 81 (2007) 552–558.

[56] Y. Zhang, et al., Meta-analysis of GWAS on two Chinese populations followed by replication identifies novel genetic variants on the X chromosome associated with systemic lupus erythematosus, Hum. Mol. Genet. 24 (2015) 274–284.

[57] P.C.L. Ferreira, F.V. Thiesen, A.G. Pereira, A.R. Zimmer, P.E. Fröehlich, A short overview on mycophenolic acid pharmacology and pharmacokinetics, Clin. Transplant. 34 (2020) e13997.

[58] S. Yokota, Mizoribine: mode of action and effects in clinical use, Pediatr. Int. 44 (2002) 196–198.

[59] C. Kato, K. Sato, A. Wakabayashi, Y. Eishi, The effects of allopurinol on immune function in normal BALB/c and SCID mice, Int. J. Immunopharmacol. 22 (2000) 547–556.

[60] S. Han, et al., Auranofin, an immunosuppressive drug, inhibits MHC class I and MHC class II pathways of antigen presentation in dendritic cells, Arch Pharm. Res. (Seoul) 31 (2008) 370–376.

[61] S.A. Stewart, et al., Lentivirus-delivered stable gene silencing by RNAi in primary cells, RNA 9 (2003) 493–501.

[62] C. Mayr, D.P. Bartel, Widespread shortening of 3′UTRs by alternative cleavage and polyadenylation activates oncogenes in cancer cells, Cell 138 (2009) 673–684.

[63] J.S. Boehm, M.T. Hession, S.E. Bulmer, W.C. Hahn, Transformation of human and murine fibroblasts without viral oncoproteins, Mol. Cell Biol. 25 (2005) 6464–6474.

[64] C. Lois, E.J. Hong, S. Pease, E.J. Brown, D. Baltimore, Germline transmission and tissue-specific expression of transgenes delivered by lentiviral vectors, Science 295 (2002) 868–872.

[65] J.B. Spinelli, et al., Fumarate is a terminal electron acceptor in the mammalian electron transport chain, Science 374 (2021) 1227–1237.

[66] K. Birsoy, et al., Metabolic determinants of cancer cell sensitivity to glucose limitation and biguanides, Nature 508 (2014) 108–112.

[67] J. Moffat, et al., A lentiviral RNAi library for human and mouse genes applied to an arrayed viral high-content screen, Cell 124 (2006) 1283–1298.

[68] P. Mali, et al., RNA-guided human genome engineering via Cas9, Science 339 (2013) 823–826.

[69] K.B. Walsh, et al., Intracerebral hemorrhage induces inflammatory gene expression in peripheral blood: global transcriptional profiling in intracerebral hemorrhage patients, DNA Cell Biol. 38 (2019) 660–669.

[70] L. Lee, R.E. Kelly, S.C. Pastra-Landis, D.R. Evans, Oligomeric structure of the multifunctional protein CAD that initiates pyrimidine biosynthesis in mammalian cells, Proc. Natl. Acad. Sci. USA 82 (1985) 6802–6806.

[71] D. Gestaut, A. Limatola, L. Joachimiak, J. Frydman, The ATP-powered gymnastics of TRiC/CCT: an asymmetric protein folding machine with a symmetric origin story, Curr. Opin. Struct. Biol. 55 (2019) 50–58.

[72] S.S. Chirala, A. Jayakumar, Z.-W. Gu, S.J. Wakil, Human fatty acid synthase: role of interdomain in the formation of catalytically active synthase dimer, Proc. Natl. Acad. Sci. 98 (2001) 3104–3108.

[73] D.M. Lawson, et al., Solving the structure of human H ferritin by genetically engineering intermolecular crystal contacts, Nature 349 (1991) 541–544.